Statistically Modified Subset Order Subset Expectation Maximization (SMS-OSEM) SPECT Image Reconstruction

By

Emebet Hailu Mamo

In Partial Fulfillment of the Requirements for the Degree of Master of Science in Biomedical Engineering

Center of Biomedical Engineering

Addis Ababa Institute of Technology

Addis Ababa University

Advisor: Dawit Assefa Haile (PhD)

December, 2020

Addis Ababa, Ethiopia

Declaration

I, the undersigned, declare that this MSc thesis is my original work, has not been presented for fulfillment of a degree in this or any other University, and all sources and materials used for the thesis have been acknowledged.

Name: Emebet Hailu Mamo

Signature: _____

Date: _____

This MSc. Thesis has been submitted for examination with my approval as an advisor.

_____

Dawit Assefa Haile (PhD)

Certificate of Examination

Addis Ababa University

School of Graduate Studies

This is to certify that the thesis prepared by Emebet Hailu Mamo entitled "Statistically Modified Subset Order Subset Expectation Maximization (SMS-OSEM) SPECT Image Reconstruction" submitted in partial fulfillment of the requirements for the degree of Master of Science in Biomedical Engineering (Biomechanics and Biomedical Rehabilitation) complies with the regulations of the University and meets the accepted standards with respect to originality and quality.

Signed by the examining committee

Examiner:	_____	Signature:	_____	Date:	_____
Examiner:	_____	Signature:	_____	Date:	_____
Advisor:	_____	Signature:	_____	Date:	_____

_____

Chief of Department or Graduate program coordinator

Abstract

Single photon emission computed tomography (SPECT) imaging is widely implemented in nuclear medicine as its clinical role in the diagnosis and management of several diseases is, many times, very helpful. The goal of reconstruction in tomographic images is as much as possible to recreate the exact image of an object being scanned. Nevertheless, the quality of the reconstructed image depends on the performance of the reconstruction algorithm. One of the most commonly used SPECT reconstruction algorithms in clinical practice is ordered subset expectation maximization (OSEM). It uses a subset of projections to shorten the reconstruction time to reach maximum reconstruction accuracy. However, only few studies are made on the use of statistical measurements to ordered subsets for better reconstruction performance. Hence, the aim of this thesis work is to develop a scheme for use in better SPECT image reconstruction in such a way that there will be improvement on the quality of the reconstructed image as well as reconstruction time. First the SPECT imaging system is simulated and projections of different phantoms (Shepp-Logan, Jaszczak, and Thorax) are calculated. Then the SPECT imaging system matrix is computed using main geometrical parameters of the SPECT instrument. Following this, the projections are grouped into subsets depending on the phantom used. The main contribution of the thesis work is that the subsets are ordered in decreasing order using statistical measurements such as variance, standard deviation and entropy. This measurement allows to find more information about the image being reconstructed. Consequently, a better and faster SPECT image reconstruction method known as Statistically Modified Subset OSEM (SMS-OSEM) is developed. The performance of the SMS-OSEM scheme was compared against the traditional OSEM by varying the number of iterations, the number of subsets and noise levels. The overall performance of the proposed algorithm was checked with different number of iterations (1, 10, 30, 50 and 100) using three different types of phantoms. Based on the phantoms tested using SMS-OSEM algorithm, it was observed that OSEM with variance based subset ordering was able to increase accuracy of the traditional OSEM reconstruction by 15.02% when the number of iterations is low between 1 and 20. For higher number of iterations, the accuracy was increased up to 67.88% depending of the phantom type. In addition, the reconstruction time was reduced by 12.52% for lower number of iterations and by 33.03% for higher number of iterations. The degree of tolerance of the SMS-OSEM method towards noise was tested by adding different amount of Gaussian noise and the algorithm offered better performance than the traditional OSEM scheme.

Keywords: Single-photon emission computed tomography, SPECT, Tomography, OSEM, Statistically modified subset, SMS-OSEM, Image Reconstruction.

Acknowledgement

My greatest thanks go to the Almighty God for the grace, courage and peace of mind that he granted me throughout the course works and during this thesis phase of my MSc degree program.

I would like to convey my sincere gratitude to my advisor Dawit Assefa (PhD) for his advice, continuous support, motivation, enthusiasm, patience, constructive comments and immense knowledge throughout the process of researching this thesis.

My grateful thanks goes to Masreshaw Demelash (PhD), Dean of the School of Multidisciplinary Engineering, for his guidance and valuable advice.

Last but not the least, I offer my regards and blessings to my husband Mulualem Alemar (MSc) for his love, care, continuous support and encouragement.

Table of Contents

List of Figures

List of Tables

List of Abbreviations

ART	**A**lgebraic **R**econstruction **T**echnique
BP	**B**ack-**P**rojection
CZT	**C**admium **Z**inc **T**elluride
CAD	**C**oronary **A**rtery **D**isease
CIED	**C**ardiac **I**mplantable **E**lectronic **D**evices
CT	**C**omputerized **T**omography
DAQ	**D**ata **A**cquisition
ECT	**E**mission **C**omputed **T**omography
ET	**E**mission **T**omography
FBP	**F**iltered **B**ack-**P**rojection
FT	**F**ourier **T**ransform
IR	**I**terative **R**econstruction
ISR	**I**ntrinsic **S**patial **R**esolution
LORs	**L**ine **O**f **R**esponses
ML	**M**aximum **L**ikelihood
MLEM	**M**aximum **L**ikelihood **E**xpectation **M**aximization
MRI	**M**agnetic **R**esonance **I**maging
PMT	**P**hoto **M**ultiplier **T**ube
RP	**R**adioactive **P**harmaceutical
ROR	**R**adius of **R**otation
SMS	**S**tatistically **M**odified **S**ubset
SNR	**S**ignal to **N**oise **R**atio
SPECT	**S**ingle **P**hoton **E**mission Computed **T**omography
SR	**S**tatistical **R**econstruction
OSEM	**O**rdered **S**ubset **E**xpectation **M**aximization
2D	**T**wo-**D**imensional
3D	**T**hree-**D**imensional

Chapter 1 Introduction

This chapter discusses background of the study, statement of the problem, research objectives, significance, scope and delimitations of the study.

1.1 Background

Single photon emission computed tomography (SPECT) is a nuclear imaging modality used by, among others, oncologists in the imaging of tumors [1]. In SPECT, patients are injected with a γ-emitter–labeled radioactive pharmaceutical (RP), which emits photons as it circulates through the bloodstream. Then an external device, the gamma camera, detects the radioactivity stemming from the body [2]. The number of photons emitted from a given location in the body depends directly on the concentration of the RP.

SPECT imaging can be used to map the patient's body as well as to measure blood flow. Medical experts have found uses for SPECT in various application areas, including epilepsy, Parkinsonism, oncology, and coronary artery diseases [1]. In SPECT the image obtained at one angle of view is the projection of the 3-dimensional (3D) distribution onto the 2-dimensional (2D) detector plane. Because of the projection operation, no information regarding the depth at which disintegrations occur is available. Moreover, activities stemming from separate structures may overlap each other on the detector plane, and the contrast may be low. With only one projection image, it is impossible to determine the activity distribution because an infinite number of distributions can yield the same projection. Consequently, to get more information about activity distribution, projections are acquired over a large number of angles of view around the subject. Thus, the basic concept of SPECT is to attain, as near as possible of an image of the γ-emitter distribution in any slice of the body, using projections of this image acquired by a rotating gamma camera from numerous angles of view [2].

During the history of the reconstruction method development, several techniques for radionuclide image reconstruction have been explored in the literature. These reconstruction techniques are classified as analytical and iterative reconstruction algorithms. Analytical reconstruction algorithms are one of the oldest methods and they can be classified into Fourier reconstruction and filtered back projection (FBP) method [3]. Whereas iterative reconstruction methods are more

recent techniques. Iterative reconstruction starts with an initial estimate of the image. Then a set of projection data is estimated from the initial estimate using a mathematical process called forward projection. The resulting projections are compared with the recorded projections and the differences between the two are used to update the estimated image. The iterative process is repeated until the differences between the calculated and measured data are smaller than a specified preselected value [4].

The iterative reconstruction methods include algebraic methods like the algebraic reconstruction technique (ART) and statistical algorithms like maximum likelihood expectation maximization (MLEM) or ordered subsets expectation maximization (OSEM) [4]. As modern computers have become more computationally powerful, iterative algorithms for reconstruction have been used in place of filtered back projection. Such processing can give better image quality compared to that of the filtered back-projection algorithm [5]. For SPECT imaging, iterative reconstruction has virtually replaced analytical reconstruction in routine clinical practices [6].

There is continued research on optimizing iterative reconstruction methods with particular interest in extending the current approaches to incorporate more exact, though increasingly complex models of the underlying systems [6]. The practical shortcoming of the iterative algorithms is their very slow convergence speed and thus a large number of iterations may be required to obtain an acceptable reconstructed image. One popular and effective method for accelerating the convergence is the use of ordered subsets [7]. The OSEM is one of such methods that make use of ordered subsets to enhance the speed of convergence of reconstruction.

The use of the OSEM method has recently gained a lot of interest in different applications. As the advantages of the OSEM method, reduction of streak artifacts from a high density area and easiness to build attenuation correction, scatter correction and the like into reconstructive soft-wares have been mentioned [8]. In recent years, the OSEM method has been widely used for clinical purposes, and many studies on the combination of the number of times of iteration and the number of subsets as well as clinical applications have been made. However, very few studies on the use order of subsets have been made [8], [9]. Various studies on the number of subsets and iterations and in the clinical use of the OSEM method have been made up to date, but studies on the use order of subsets have been scarcely made. Thus, the current thesis study focuses on the use order of subsets by

reordering the subsets and the use order of subsets of the different phantom images as the study's subject images [8].

1.2 Statement of the Problem

Practical limitation of the iterative algorithms is their sluggish speed of convergence. As a result, large number of iterations may be essential to attain a satisfactory reconstructed image. For the purpose of speeding up iterative reconstruction, OSEM and its variations have been developed in the literature. However, only few studies are made on the use statistical measurements to ordered subsets for better reconstruction performance. In OSEM reconstruction, the order of subsets plays a big role and the important question to ask is how the subsets should be ordered in order to get a much faster and more realistic reconstructed image. Hence, the aim of this thesis study is to thoroughly investigate a better way of ordering subsets so that efficient reconstruction is made within a short time.

1.3 Objectives of the Thesis

1.3.1 General Objective

The main objective of this thesis is to investigate a special subset reordering technique in order to achieve a more realistic iterative SPECT image reconstruction with less number of iterations.

1.3.2 Specific Objectives

The specific objectives of this thesis are to:

- Simulate a SPECT imaging system;
- Compute SPECT imaging system matrix;
- Find a better way of reordering of subsets to shorten reconstruction time;
- Quantify the accuracy and reconstruction time;
- Compare modified OSEM with ordinary OSEM algorithm with respect to reconstruction time and accuracy.

1.4 Significance of the Thesis Study

Application of SPECT imaging is now a common practice in medical diagnostics. Imaging using SPECT technique is increasingly being used in clinical nuclear medicine such as oncologic imaging, malignant and benign bone diseases, infection imaging, and myocardial perfusion

imaging. The findings of the current study could lead to a better and quicker iterative reconstruction algorithm. A faster and accurate algorithm means more patients are diagnosed properly thereby reducing misdiagnosis scenarios.

1.5 Scope and Delimitations of the Thesis

The thesis only considers and models a SPECT imaging system with parallel hole collimators when computing system probability matrix. In addition, the computational reconstruction time is computed for a SPECT imaging system with 32 detectors and image size of 32x32. Analysis on effects of attenuation, or scatter of photons on the reconstruction and the model of divergent or convergent type of collimators is beyond the scope of the current thesis study.

1.6 Organization of the Thesis

The rest of the thesis has been organized into the following chapters. In Chapter 2, the basic concepts and instrumentation of SPECT imaging are discussed. Chapter 3 provides a description on different SPECT image reconstruction methods available in the literature. Chapter 4 explains the methodologies and procedures proposed in this thesis for an effective and faster SPECT image reconstruction. Chapter 5 presents selected results accompanied by useful discussions. Supplementary results are also included in appendices A and B. Chapter 6 offers a summary and discussion of the research findings in this thesis, their implications as well as recommendations for possible future studies.

Chapter 2 SPECT Imaging

In this chapter image formation by a single-photon emission computed tomography (SPECT) is discussed. It begins with SPECT imaging instrumentation components and states advantages and application areas of SPECT imaging.

2.1 Background

The origin of SPECT can be found in the groundbreaking experiments on emission tomography performed approximately 65 years ago by David Kuhl and Roy Edwards [10]. In 1964, the research group of Dr. David E. Kuhl, known as the "Father of Emission Tomography", developed the Mark II SPECT series, which is a single-emission computed tomography camera. The continuous development of SPECT over the past decades has led to remarkably improved image quality and increased diagnostic confidence [11]. A typical SPECT scanning machine is shown in Fig. 2-1.

Figure 2-1: Typical SPECT imaging system [11].

Throughout a SPECT scan, the detector moves along an orbit around a patient and acquires data via either a continuous or a stop-and-shoot technique. The mechanical axis of rotation must be fixed in space during the scan. The radius of rotation (ROR) can be fixed or variable. As a result, a series of planar images called projections is created. This projection set is reconstructed into the expected 3-D distribution of radiotracer or activity inside the patient. The function of the gamma

camera system is to capture the gamma radiation that has been emitted from the patient and convert it into useful information that can be reconstructed into the activity distribution.

The basic operation of this system is as follows: First, the gamma radiation emitted from the patient is mechanically directed by means of an aperture or a collimator towards a scintillation crystal (see Fig. 2-1). This is achieved by absorbing radiation that is propagating in directions other than that specified by the collimator. There are tradeoffs between collimator resolution and sensitivity that depend on its geometry. From the selected photons that reach the scintillation crystal, only a very small fraction ($\sim 10^{-4}$) interacts with it and converts its energy into scintillations and consequently into electronic pulses [6].

2.2 Major Components of SPECT

The two main components of a SPECT system are the detector and the collimator system. These two important systems interact with and complement each other in many ways. It would be a fault to consider either of the two without keeping the other also in mind [2].

2.2.1 Detectors

Detectors are the core of a SPECT system and are responsible for collecting the high-energy photons emitted by the patient, estimating the photon energy and location of interaction, and generating count data for ensuing image reconstruction. The ability to perform these duties depends on their design, materials, and electronics. Energy resolution, camera sensitivity, and spatial resolution are the primary variables that dictate the performance of a SPECT detector [21]. A schematic of a gamma camera is shown in Fig. 2-2.

The projection information required for SPECT is acquired by g-ray detectors, and much of the quality of the projection depends on the properties of these detectors. We desire detectors with the following characteristics: (a) high intrinsic efficiency, (b) good energy resolution, and (c) good intrinsic spatial resolution. Materials with high atomic numbers and high density are important for detector efficiency. Both energy resolution and spatial resolution depend on the size of the signal generated with each detected event [22].

The detector system includes three subcomponents: conversion medium, sensors, and data acquisition (DAQ) system. The first two comprise the detector. The conversion medium is made of high-Z and high density material that stops photons and converts the energy transferred to measurable form, such as carriers of electric charge or scintillation light. The sensors collect these

carriers to generate the electric signals that are passed on to the DAQ. The DAQ then processes these signals in real time to derive the spatial coordinates of interaction location along with the energy absorbed from the detected event [22], [23].

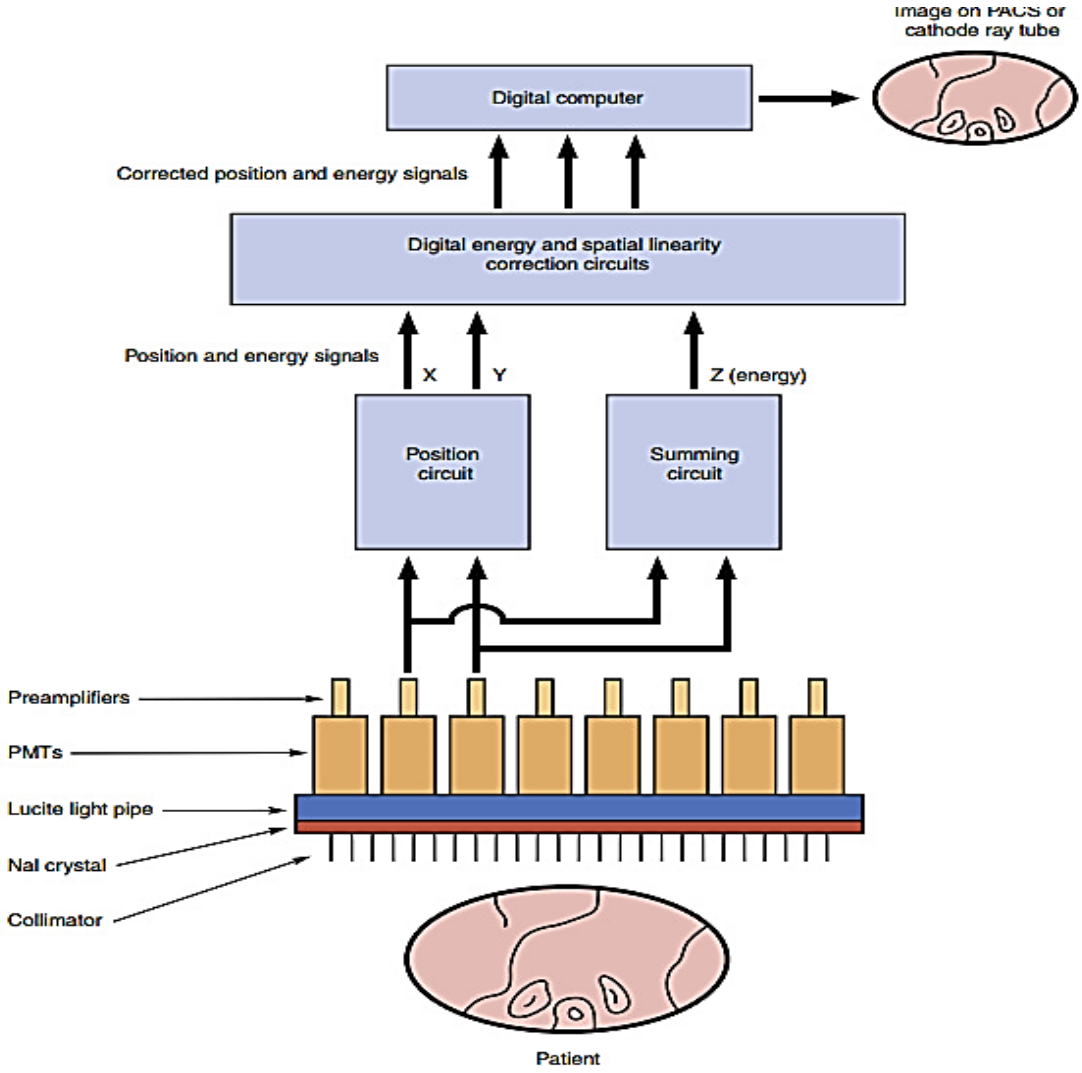

Figure 2-2: Gamma camera schematic. A cross-sectional image of the patient is shown at the bottom, with a final image seen on the computer console at the top [4].

The intrinsic spatial resolution (ISR) of conventional Anger camera systems has long been in the 3–4 mm range. Further improving their ISR is generally not cost-effective, because the hardware resolution of a system is mainly limited by the much poorer collimator resolution in the typical imaging distance. However, the design concept of using projection minification in SPECT systems requires new detectors of high ISR to optimize system design and performance. To facilitate

special detection geometries, small modular detectors without the dead regions along the detector edges associated with Anger-type cameras are also needed. As a result, several new detectors have been introduced in SPECT systems in the last decades. Detectors in SPECT systems can be divided into three types: monolithic scintillator based, pixelated scintillator based, and pixelated CZT based [23].

2.2.2 Gamma Scintillation Camera

The majority of SPECT systems are based on Anger camera technology where one or more cameras rotate about the body of the patient. Anger cameras consist of a single crystal, which absorbs incident gamma photons and scintillates or emits light in response, and in back of which are banks of photomultiplier tubes and electronics to compute gamma ray energy and the location of scintillation within the crystal. Anger camera NaI (Tl) crystals are typically 1/4 to 3/8 inches thick, although they may be as thick as 5/8 inches. The thicker the crystal, the greater the sensitivity of the Anger camera, because of the increased probability that a gamma ray passing through the crystal will interact. However, the thicker the crystal, the greater the spread of the emitted light photons produced from the scintillation, and the less precise the computation of gamma ray interaction location resulting in poorer intrinsic resolution of the camera [21], [23].

However, several advantageous features of Anger cameras for general-purpose imaging become weaknesses when it comes to special-purpose applications. The large size of the detectors is not really optimal for most clinical imaging, because body contours are mostly curved and convex, which make it difficult, if not impossible, for most of the detector area to maintain close proximity for effective collimation. Curved detector geometries are best facilitated with an assembly of small modular detectors. An example is the curved detectors used in SPECT systems, which are assembled from a large number of small and identical modular detectors. However, conventional anger camera technology cannot accommodate small and modular detectors efficiently, because it inherently comes with dead, or non-position-sensitive regions, which are about half a photo multiplier tube (PMT) width all around the edges of each crystal slab [23].

2.2.3 Pixelated Scintillator-Based Detector

An array of scintillation crystals is an alternative to the single-crystal Anger camera design. A large number of small crystals (e.g., 6 mm CsI (Tl) cubes) are coated with reflective material and

packed into an array. An advantage of this pixelated design is that the scintillation light is much more focused than in an Anger camera and can be detected by a photodiode array instead of conventional PMTs, thereby making the detector much more compact. A possible concern for pixelated detectors is that their less efficient light collection may degrade energy resolution. Pixelated detectors are capable of very high counting rates due to their isolated light pulses and have been used in first-pass cardiac scintigraphy [21].

2.2.4 Semiconductor Detectors

Pixelated semiconductor (solid-state) detectors using CZT crystals have been a focus of interest for more than 20 years (Barber and Woolfenden 1996) [23]. Those semiconductor detectors are solid state devices that provide direct conversion of absorbed g-ray energy into an electronic signal. Because there is no need for an intermediate high-gain amplification stage, these devices are compact and operate at low voltage. The absorbed energy from a γ-ray interaction liberates charge carriers (electrons and holes) within the charge-free depletion zone of the semiconductor [22].

In solid-state detectors, gamma rays are absorbed into the semiconductor material which directly generates electron-hole pairs which are pulled to the end plates through an applied electric field. The collected charge from the electron-hole pair is used to determine the location and energy of the gamma ray. One such solid-state detector is made of cadmium zinc telluride (CZT), and SPECT devices utilizing these detectors have been reported to provide improved count sensitivity, superior energy resolution, and finer spatial resolution.

The magnitude of improvement that has been reported consists of simultaneously acquiring three to ten times more counts, with over two times better spatial resolution than the Anger camera. The small size of solid-state modules has made a number of innovative detector designs possible. Some devices now have static arrangements of CZT crystals, and the only moving part is a collimator array. Other arrangements of CZT detectors have each detector module equipped with its own pinhole collimator, for which there are no moving parts other than a mechanism to move the detector as close as possible to the patient [21].

Properties of a typical nuclear medicine imaging equipment are listed in Table 2-1.

Table 2-1: Properties of Typical Nuclear Medicine Imaging Equipment [5].

Characteristic	**SPECT Gamma Camera**
Radionuclides imaged	Any with gamma or x-ray in the energy range 40-520 keV
Collimators	Low energy all-purpose and high resolution, medium and high energy, pinhole
Detector	Rotating dual head with various configurations, including noncircular orbits
Crystal material	Sodium iodide crystal (thallium doped) usually single
Crystal size	60 × 50 cm
Crystal thickness	9.5 mm (3/8 inches) or 15.9 mm (5/8 inches)
Photomultiplier tubes	40-90
Spatial resolution (intrinsic)	3-10 mm (varies with type of reconstruction)
Energy window	40-520 keV (capable of six energy windows simultaneously)
Field uniformity	2%-5%
Maximum count rate	300-350 kcps
Axial resolution (FWHM)	8-9 mm FWHM (low energy all-purpose collimator)
Energy resolution (FWHM)	≤10%

2.2.5 Collimator

The collimator is made of perforated or folded lead and is interposed between the patient and the scintillation crystal. It allows the gamma camera to localize accurately the radionuclide in the patient's body. SPECT image reconstruction requires that the incident direction of each acquired count be known. An external collimator is used to do so, by absorbing photons outside a range of incident angles as specified by the collimator design [21]. Collimators perform this function by absorbing and stopping most radiation except that arriving almost perpendicular to the detector face as shown in Fig. 2-3.

Collimator septa are composed of highly absorbing material, that is, material that has a high atomic number and a high density. Alloys of lead are the most common septal materials. Alloys of tungsten and gold are also used, but not widely, because tungsten is difficult to work and gold is relatively expensive [24], [25]. Most radiation striking the collimator at oblique angles is not included in the final image. Of all the photons emitted by an administered radiopharmaceutical,

more than 99% are “wasted” and not recorded by the gamma camera; less than 1% are used to generate the desired image. Thus the collimator is the “rate limiting” step in the imaging chain of gamma camera technology. Collimators with various hole shapes—circular, square, triangular, or hexagonal—have been developed. Hexagonal holes are the most common because they are generally the most efficient [24].

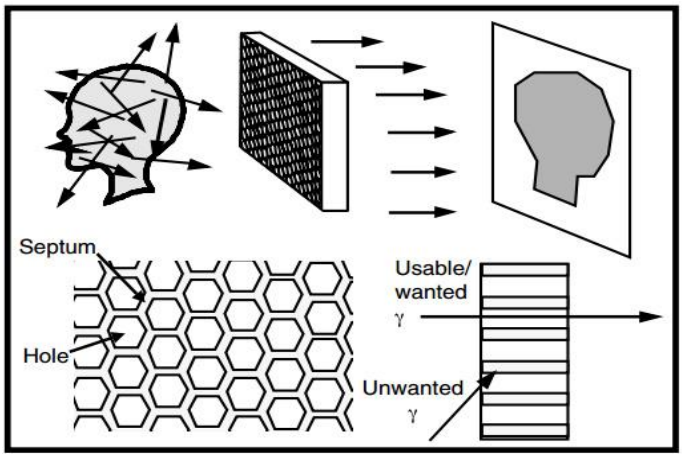

Figure 2-3: Hexagonal parallel-hole collimator. A parallel-hole collimator is a mechanical selector of gamma photons. It passes what become usable photons, photons that enter the crystal from known directions. The collimator absorbs most other photons those that interact with septa [1].

Collimator Types

Collimators can be divided into two major groups based on their image formation process or collimation geometry: pinhole collimator and multichannel collimator. The very first collimator used by Anger in the development of the scintillation camera was a pinhole collimator [22]. It provides a diverging collimation geometry that all incoming photons pass through a circular pinhole of a few millimeters at the front end of the collimator. Its focal length, defined as the distance from the pinhole to the detector plane along the central axis of the pinhole, usually varies with detector size and is typically in the range of 5-20 cm [23]. Pinhole collimator operates in a manner similar to that of a box camera. Radiation must pass through the pinhole aperture to be imaged, and the image is always inverted on the scintillation crystal. Because little of the radiation coming from the object of interest is allowed to pass through the pinhole over a given time period, the pinhole collimator has very poor sensitivity.

Collimator sensitivity refers to the percentage of incident photons that pass through the collimator. The poor sensitivity of a pinhole collimator makes placement near the organ of interest critical, and bringing the object of interest close to the pinhole magnifies the image. Because magnification

is a function of distance, if the object of interest is not relatively flat or thin, the image may be distorted. Pinhole collimators are routinely used for very high resolution images of small organs, such as the thyroid, and for certain skeletal regions, such as hips or wrists, especially in pediatric patients [25]. Collimators with different energy and sensitivity level are shown in Table 2-2.

Due to the limitation of pinhole collimation for clinical imaging, multichannel collimators were developed [26]. Multichannel collimators pack a large array of narrow mechanical channels in a slab of finite thickness. Depending on the relative orientation of the channels, they can be divided into three subgroups: parallel, converging, and diverging; each is characterized by its focal length, which is ∞, >0, or <0, respectively. Among them, parallel-hole collimators are the most widely used [5]. All their sampling lines are parallel and typically normal to the collimator's surface [23], [25].

Table 2-2: Performance characteristics of some typical commercially manufactured collimators [24].

Collimator Type	**Recommended Max. Energy (keV)**	**Efficiency, g**	**Resolution Rcoll (FWHM at 10 cm)**
Low-energy, high-resolution	150	1.84×10^{-4}	$7.4mm$
Low-energy, general-purpose	150	2.68×10^{-4}	$9.1mm$
Low-energy, high-sensitivity	150	5.74×10^{-4}	$13.2mm$
Medium-energy, high-sensitivity	400	1.72×10^{-4}	$13.4mm$

The structure of a parallel-hole collimator is similar to that of a honeycomb, consisting of a large number of narrow channels separated by thin septa. The lead walls between the holes are referred to as *septa.* The septa absorb most gamma rays that do not emanate from the direction of interest; therefore a collimator for high energy gamma rays has much thicker septa than does a collimator for low energy rays. The septa are generally designed so that septal penetration by unwanted gamma rays does not exceed 10% to 25%. The range of incident angles passing through the collimator depends on the channel width and length. The septa must be thick enough to absorb photons of the desired energy in order to accept photons that are incident on the collimator within a range of directions. Collimators are often categorized as low-, medium-, or high-energy depending on the photon energy for which the collimator is designed. Various designs of low-energy collimators are classified as high-resolution, all-purpose, high-sensitivity, etc., depending

on the collimator's angle of incidence [21]. The three collimator geometries: convergent, parallel and divergent are shown in Fig. 2-4.

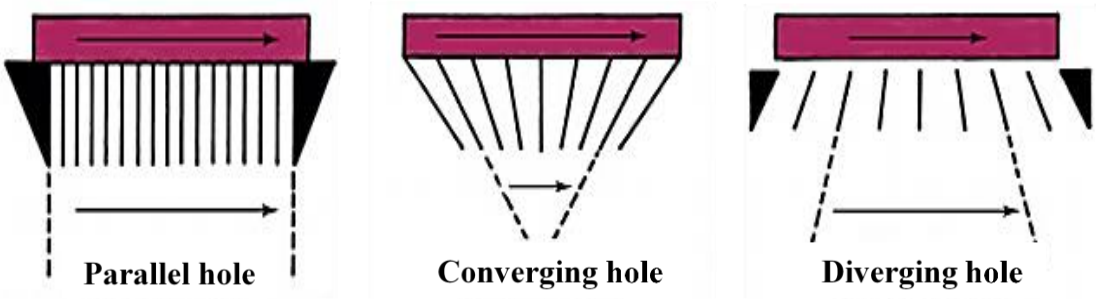

Figure 2-4: Types of gamma camera collimators. As the energy of the radionuclide increases, the best collimator usually has thicker and longer septa. For a given septal thickness, spatial resolution of a collimator increases with septal length but sensitivity decreases [27].

Examples of two clinical SPECT scanners are shown in Fig. 2-5 [23]. The two gamma camera heads are mounted on a rotating gantry that is separate from the high-speed slip-ring system.

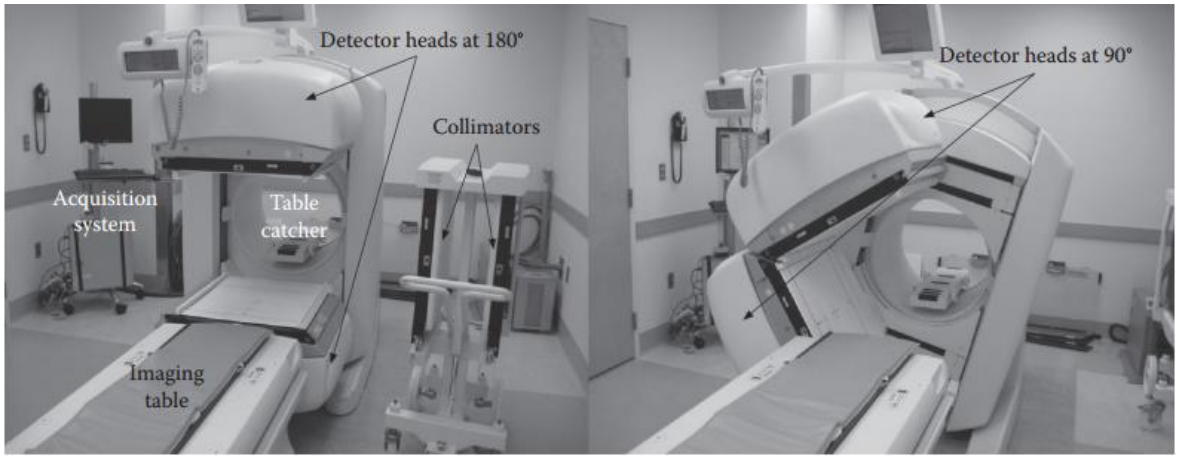

Figure 2-5: Modern two-headed SPECT systems shown in two different configurations of the detector heads (180° to the left and 90° to the right) [2].

2.3 Mechanical System

SPECT systems have complex set of mechanical components, which form the backbone of the system. The accuracy and precision, as well as reliability and reproducibility, of their operations are essential. The mechanical system consists of two parts: the gantry, which holds all subsystems together and enables their joint operation, and the motion system, which provides motion to complete data sampling and detection geometry [23].

2.3.1 Gantry System

Usually, clinical SPECT systems use a conventional circular gantry, similar to x-ray CTs, with its central axis horizontally oriented. The gantry is the mounting frame, and often the housing for detector and collimator systems, which are arranged on the transverse plane around a patient lying on a couch along the long axis. The gantry has a mechanical motion system to achieve motion of its detector or collimator systems with multiple degrees of freedom to provide desired detection geometries. The detector system and collimator system can be either integrated in the same unit or separated as two independent components. Although the number of detectors or camera heads varied in early years, only single-head and dual-head systems remain on the current market for general-purpose imaging [23].

2.3.2 Motion System

The major function of the motion system is to provide a sufficient number of different projection images of the imaging volume to meet angular sampling requirements. Most SPECT systems have a motion system that varies in complexity. This system includes a series of mechanical components under computer control to rotate its detector or collimator to acquire multiple trans-axial projections sequentially over an angular range of the imaging volume. The current general-purpose SPECT systems, such as dual-head systems, use a heavy-duty motion system to rotate the cameras on a vertically oriented transverse plane around a patient lying on the couch.

Additional kinds of motion have been introduced as SPECT systems evolve. Examples are the radial motion of the camera heads for body contouring, translational motion of the gantry or the couch in synchrony with detector motion, sweeping motion of line sources for transmission imaging, and translational motion to move the target into an imaging volume. Providing motion capability in SPECT systems is a complex engineering challenge, due to heavy and bulky hardware, the required precision and reproducibility, and most importantly, patient safety. Mechanical motion is not desirable in SPECT systems from the point of view of system's design, operation, maintenance, and cost. In fact, motion also prolongs imaging time and limits temporal resolution. Therefore, SPECT systems with little motion are often preferred [23].

2.4 Advantages of SPECT Imaging

SPECT imaging has several advantages which include improved contrast and reduced structural noise, due to elimination of overlapping structures. SPECT provide the only non-invasive technique for imaging brain neurochemicals. Localization of defects is more detailed and more clearly seen. Magnitude and size of defect is better defined. The higher SPECT half-life afford longer synthesis times and greater flexibility in relation to administration of radiotracers. SPECT is available in both developing and developed countries because of lower equipment cost and greater accessibility of SPECT radionuclide [12], [13].

Other important advantages of SPECT are that it has been extensively validated and has a good sensitivity, compared to other methods of assessment of myocardial viability. In addition, cost of SPECT is lower than PET (positron emission tomography) imaging and is more widely available than PET in most regions. SPECT can be used in the presence of cardiac implantable electronic devices (CIED) while cardiac magnetic resonance (CMR) imaging has important limitations in such settings [12], [14].

2.5 SPECT Imaging Application Areas

SPECT has been applied and its clinical benefits have been demonstrated across a wide spectrum of applications primarily related to blood flows to tissues and organs. This application areas include diagnosis of seizures, stroke, stress fractures, infections, and tumors in the different parts of the body. Moreover, compared to magnetic resonance imaging (MRI) and computerized tomography (CT) scanning, tests have shown that it might be more sensitive to brain injury because it can detect reduced blood flow to injured sites. In addition SPECT scanning is also useful for pre-surgical evaluation of medically uncontrolled seizures. Main application areas are discussed below [11], [15].

2.5.1 Myocardial Perfusion Imaging

Myocardial perfusion imaging (MPI) is a form of functional cardiac imaging, which illustrates the functions of the heart muscles. It is commonly performed SPECT procedure to diagnose patients with known or suspected coronary artery disease (CAD). The underlying principle is that under conditions of stress, diseased myocardium receives less blood flow than normal myocardium. MPI

is one of several types of cardiac stress tests. CAD is the number one cause of cardiovascular morbidity and mortality. MPI is useful in evaluation of coronary artery diseases, risk stratification and pre-surgical guidance, determines ischemic myocardial tissue through rest and stress cardiac studies [11], [16]. Myocardial perfusion images of stressed and rested heart are shown in Fig. 2-6.

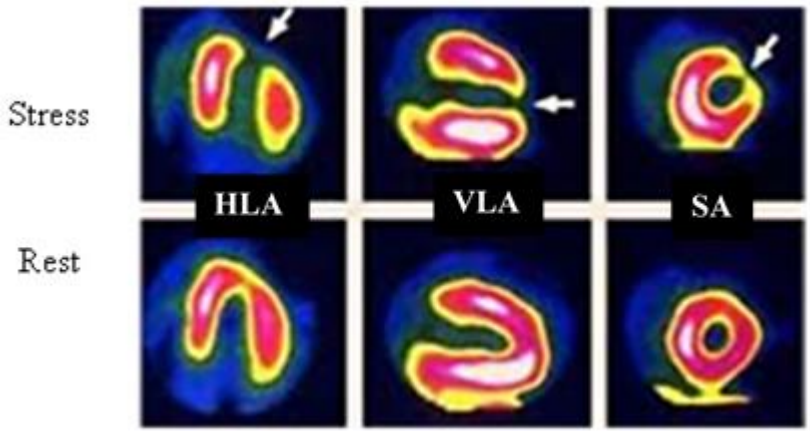

Figure 2-6: Stress and rest myocardial perfusion SPECT in horizontal long axis (HLA), vertical long axis (VLA) and the short axis (SA). There is an inducible perfusion abnormality in the left anterior descending territory, with transient ischaemic dilation of the left ventricular cavity and apparent reduction in right ventricular counts in the rest images (indicating globally reduced left ventricular counts in the stress images) [11].

2.5.2 Functional Brain Imaging

There are numerous ways to examine the brain with SPECT technology. Because blood flow in the brain is tightly coupled to local brain metabolism and energy use, SPECT is the right tool to diagnose brain. Depending on the chosen tracer, nuclear medicine examinations can diagnose dementia, cerebrovascular diseases, epilepsy, Parkinson's disease and cerebral death [16]. SPECT imaging of brain perfusion is performed in cases of dementia and epilepsy. More recent studies have shown the accuracy of SPECT in Alzheimer's diagnosis which may go as high as 88% [17]. In meta-analysis, SPECT was superior to clinical exam and clinical criteria (91% radiotracer sensitivity vs. 70% sensitivity) in being able to differentiate Alzheimer's disease from vascular dementias [18]. A brain SPECT scan of a patient with uncontrolled complex partial seizures is shown in Fig. 2-7.

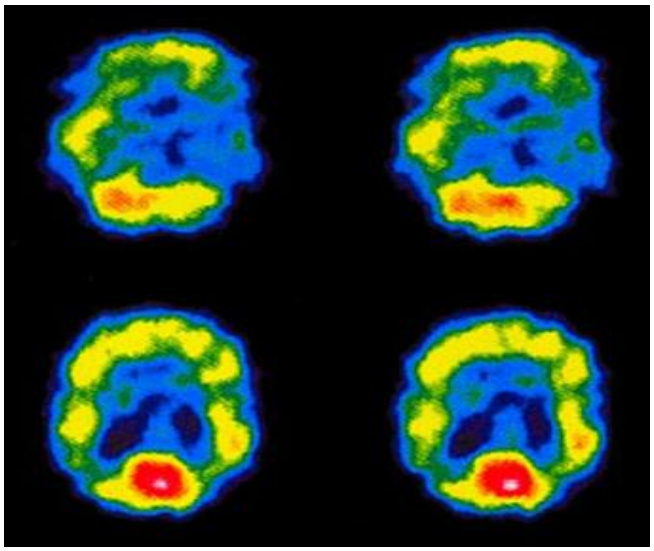

Figure 2-7: A SPECT scan of a patient with uncontrolled complex partial seizures. The temporal lobe on the left side of the brain shows less blood flow than the right, confirming for the surgeon the nonfunctioning area of the brain causing seizures. Ictal SPECT (upper) interictal SPECT (lower) and lowest activity (left) and highest activity (right) [17].

There are also other application areas where SPECT imaging has been found useful. Diagnosis of liver and pancreas functions, brain metabolism and neurochemistry, kidneys and adrenal glands, lymphoscintigraphy, prostascintigraphy, lung ventilation, perfusion and cancer detection are some of the applications while more detailed applications can be found in literatures [19], [20]. The next chapter presents literatures on SPECT image reconstruction techniques such as analytic and iterative reconstruction methods.

Chapter 3 Literature Review

In this chapter, various analytical and iterative techniques used to reconstruct SPECT images are discussed. The analytical techniques include Fourier transform method, simple back-projection and filtered back-projection while algebraic and statistical (maximum-likelihood expectation-maximization and ordered subset expectation maximization) are discussed under the iterative category.

3.1 SPECT Image Reconstruction

The Greek word "tomos" means a section, a slice, or a cut and "grapho" means to write. Hence, the scientific word tomography is a noninvasive imaging technique that is used to generate cross-sectionals images of a three dimensional (3D) object [4], [27]. Images of the inside of the human body can be obtained noninvasively using tomographic acquisition and processing techniques. In nuclear medicine, the interest is in reconstructing a cross-sectional image of radioactive isotope distributions after its administration within the human body [28]. Photon emission computed tomography provides 3D image information about the radionuclide injected into the patient that shows the metabolic and physiological activities within an organ [5]. The reconstruction of images from multiple projections of the detected emissions from radionuclides within the body is known as emission computed tomography (ECT) [25].

In tomographic techniques, projections are acquired from many different angles around the body by one or more rotating detectors (gamma cameras). These data are then reconstructed and put together to form 3D images of the body [2], [4]. In single photon emission tomography (SPECT), the basic problem of image reconstruction is to estimate a volumetric radioactive distribution from a set of two-dimensional projections [29].

There are diverse methods of image reconstruction and generally they are categorized as analytic and iterative. Analytic reconstruction methods offer a direct mathematical solution for the formation of an image. Whereas iterative methods are based on a more complicated mathematical solution requiring multiple steps to arrive at an image [29].

In this chapter image acquisition and general overview of analytic and iterative methods of reconstruction in SPECT are presented with a special focus on widely used iterative reconstruction algorithms in practice, maximum likelihood expectation maximization (ML-EM), and Ordered subset expectation maximization algorithms (OS-EM).

3.2 SPECT Image Acquisition

ECT has been widely employed in biomedical research and clinical medicine during the last three decades [4], [30]. SPECT imaging techniques employ radioisotopes which decay emitting predominantly a single gamma photon. When the nucleus of a radioisotope disintegrates, a gamma photon is emitted with a random direction. Typically, lead collimator plates are placed prior to the detector's crystal that will guide the photons to the desired direction and strike the photon detector [30].

SPECT systems use one or more gamma cameras mounted on a gantry so that the detector can rotate around the patient. From the acquired one dimensional projection data from different views around the object, two dimensional (2D) planar projection images are obtained in many evenly spaced angles around the patient as shown in Fig. 3-1 and provide an estimate of 3D distribution of the radiotracer using image reconstruction from multiple projections [4], [29].

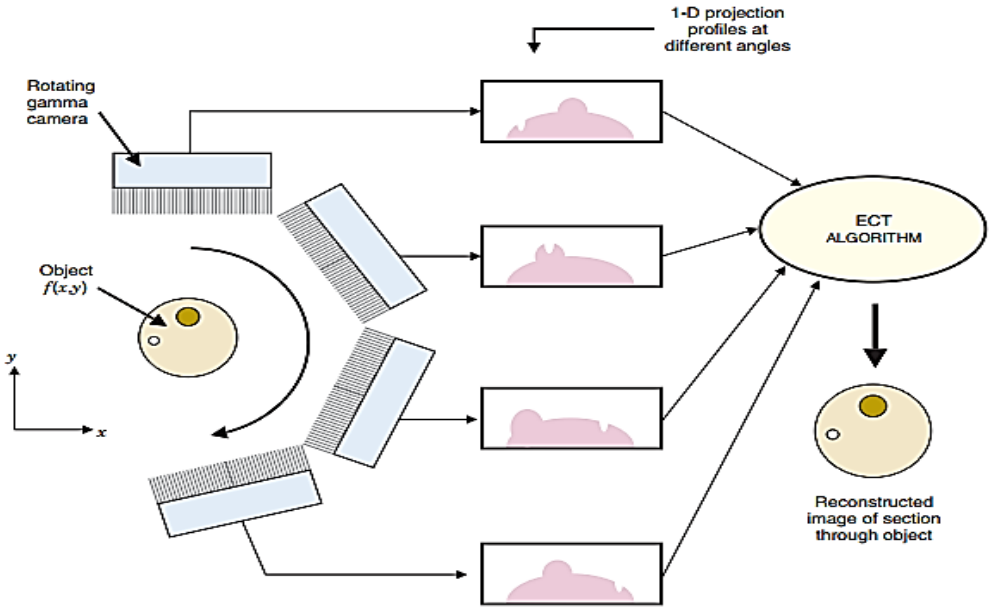

Figure 3-1: Rotating the gamma camera around the object provides a set of one-dimensional projection profiles for a two-dimensional object, which are used to calculate the two-dimensional distribution of radioactivity in the object [31].

3.3 Analytical Image Reconstruction

Analytical approaches are based on inverting the mathematical relationships between a function and its line integrals or projections. 2D image reconstruction is equivalent to the mathematical problem of recovering a 2D function from its line integrals or projections, which are often referred to collectively as the sinogram [23].

Data acquisition in SPECT involves the counting of coincident single gamma rays. The limited number of these events detected in a single scan results in photon-limited noise in the data. The Poisson distribution of this noise is not explicitly modeled in the analytical reconstruction methods. In addition, the physics of SPECT event detection limits the accuracy of the line integral model implicit in analytical methods [23].

Analytic methods typically neglect noise and complicated physical factors in an effort to obtain frameworks that yield explicit inversion formulas for the reconstruction problem. However, analytic methods usually produce solutions that are relatively practical to compute and provide insight about data-acquisition issues such as sampling [26]. In this section, the most commonly used analytical reconstruction techniques such as Fourier Transformation (FT) method, Back-Projection (BP) and Filtered Back-Projection (FBP) methods are discussed.

3.3.1 Basic Conceptions of Reconstruction

3.3.1.1 Projection and Sinogram

In SPECT, as a gamma-camera rotates in small steps around a patient, it creates a series of planar images called projections. The collection of all projections for $0 \leq \theta < 2\pi$ forms a two-dimensional (2D) matrix $p(r, \phi)$, this representation is known as sinogram. This 2D matrix is named sinogram because fixed point in the object located at a specific point (x, y) traces a sinusoidal path in the projection space [25], [29]. A sinogram for a simple point-source object is shown in Fig. 3-2. The 2D matrix rows represent an intensity display across a single projection. The successive rows from top to bottom represent successive projection angles. The sinogram provides a convenient way to represent the full set of data acquired during a scan and can be useful for determining the causes of artifacts in SPECT. A sinogram for a general object will be the superposition of all sinusoids corresponding to each point of activity in the object. Thus, the aim of the reconstruction process is to retrieve the radiotracer spatial distribution from the projection data [29].

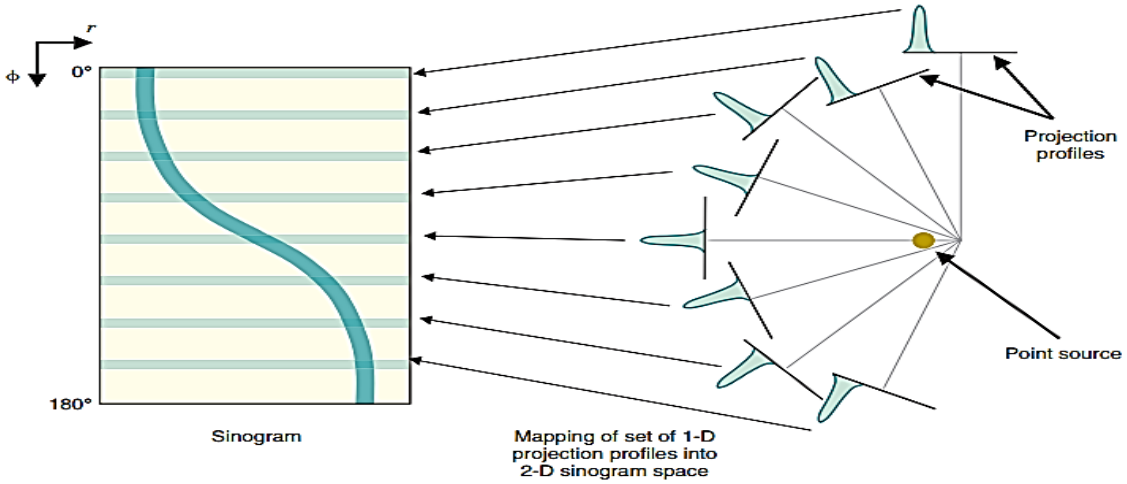

Figure 3-2: Two-dimensional (2-D) intensity display of a set of projection profiles, known as a sinogram. Each row in the display corresponds to an individual projection profile, sequentially displayed from top to bottom. A point source of radioactivity traces out a sinusoidal path in the sinogram [25].

3.3.1.2 Radon Transform

Mathematically a projection is formed by combining a set of line integrals [30], [31]. In the strict sense of the word, projections are a set of measurements of the integrated values of some parameter of the object-integrations being along straight lines through the object and being referred to as line integrals. A line integral, as the name implies, represents the integral of some parameter of the image along a line as illustrated in Fig. 3-3 [28].

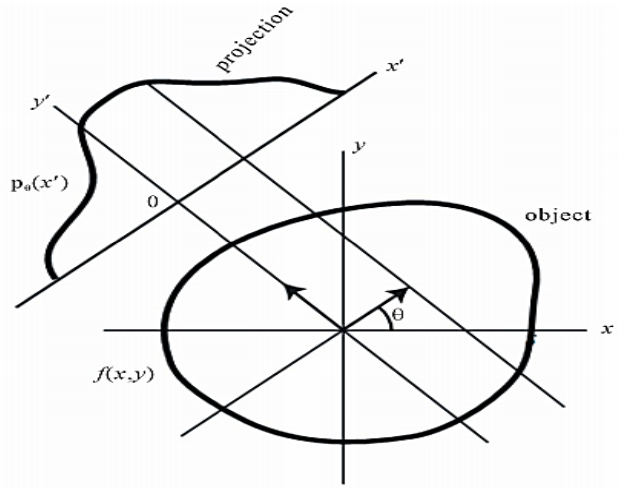

Figure 3-3: Illustration for Radon transform.

The Radon transformation shows the relationship between the two-dimensional object and the projections and guarantees that a two-dimensional object is reconstructed from projections

obtained by the rotational scanning. Radon transform is a projective transformation of a two-dimensional function onto the polar coordinate space (x', θ) and is given as:

$$P_\theta(x') = \iint_{-\infty}^{+\infty} f(x,y)\delta(x\cos\theta + y\sin\theta - x')dxdy \tag{3.1}$$

In order to express projection by an integral of one variable the rotated coordinate (x', y') by an angle θ can be expressed as follows:

$$\begin{aligned} x' &= x\cos\theta + y\sin\theta \\ y' &= -x\sin\theta + y\cos\theta \end{aligned} \tag{3.2}$$

Then,

$$P_\theta(x') = \iint_{-\infty}^{+\infty} f(x',y')dx'dy' \tag{3.3}$$

3.3.1.3 Central Slice Theorem

The central slice theorem also known as Fourier slice theorem is the most vital relationship in analytic image reconstruction [26]. This theorem relates the 2D image with its 1D projections in the Fourier domain [27]. In other words it equates the 2D Fourier transform $F(\omega_x, \omega_y)$ of $f(x,y)$ to the 1D Fourier transform $P_\theta(\omega)$, with respect to the x' coordinate, of the Radon transform $p(x', \theta)$, as illustrated in Fig. 3-4.

The 1-D Fourier transformation of the projection is:

$$P_\theta(\omega) = \iint_{-\infty}^{+\infty} f(x',y')e^{-i\omega(x')}dx'dy' \tag{3.4}$$

The 2-D Fourier transform of $f(x,y)$, $F(\omega_x, \omega_y)$ is:

$$F(\omega_x, \omega_y) = \iint_{-\infty}^{+\infty} f(x,y)e^{-i(\omega_x x + \omega_y y)}dxdy \tag{3.5}$$

where, $\omega_x = \omega\cos\theta$ and $\omega_y = \omega\sin\theta$.

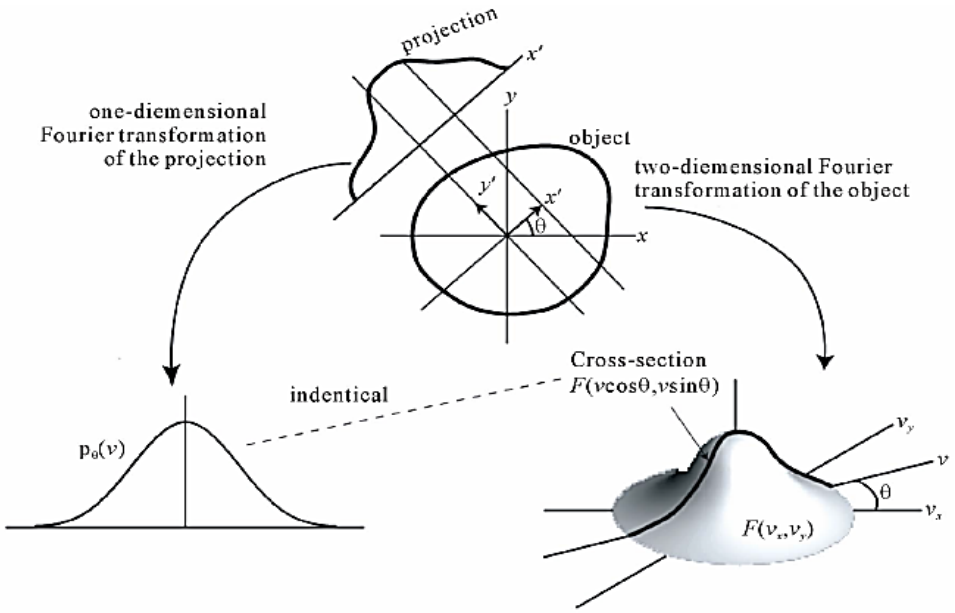

Figure 3-4: Illustration of Fourier slice theorem.

Then, the equation showing Fourier slice theorem is as follows:

$$F(\omega_x, \omega_y) = \iint_{-\infty}^{+\infty} f(x,y) e^{-i\omega(x\cos\theta + y\sin\theta)} dxdy \tag{3.6}$$

This result shows that the 1D Fourier transform of the Radon transform at angle θ gives a slice of the 2D Fourier transform of the image at the same angle θ [23].

3.4 Analytical Image Reconstruction Methods

3.4.1 Fourier Transformation (FT) Method

According to the central slice theorem, the projection of an object at an angle θ gives one cross section of the Fourier transform of the initial object, $F(\omega_x, \omega_y)$. Hence considering all projection of angle θ yields the entire profile of $F(\omega_x, \omega_y)$. Therefore it is possible to reconstruct the object $f(x,y)$ by applying the inverse Fourier transformation of $F(\omega_x, \omega_y)$. This technique is known as the Fourier transform method (see Fig. 3-5) [25], [29], [32].

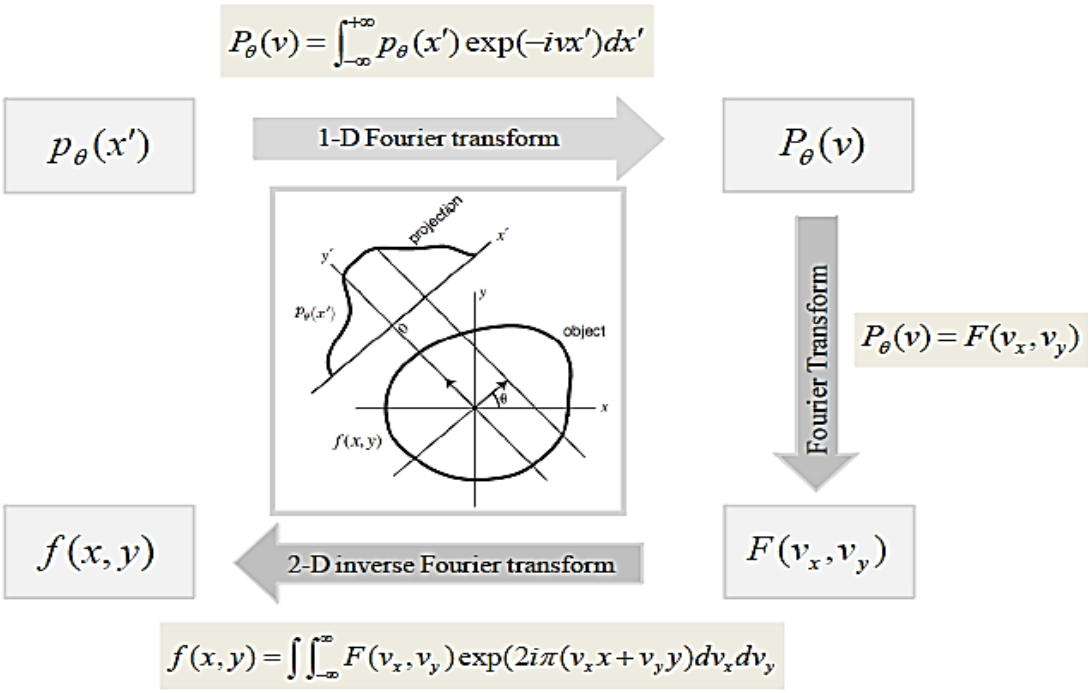

Figure 3-5: Flow of direct Fourier transform reconstruction.

3.4.2 Simple Back-Projection (BP) Method

Back-projection denotes the accumulation of the ray-sums of all the rays that pass through any point (x, y). Applying backprojection to projection data is known as summation algorithm [2], [28]. Back-projection is done between 0 and π radians. Since, projections obtained between π radians (180°) and 2π radians (360°) are symmetric with projections acquired at angles between 0 and π, projections attained at angles between a radian (180°) and 2 radians (360°) do not provide new information. Detailed back projection reconstruction mathematics can be found in [29]. For point source (delta function), $f(x, y) = \delta(x, y)$, the final reconstructed image by back projection is given as:

$$bp(x,y) = \iint_{-\infty}^{+\infty} \delta(x,y) \left[\frac{1}{\sqrt{(\alpha - x)^2 + (\beta - y)^2}}\right] d\alpha d\beta \qquad (3.7)$$

The equation has a blurring factor $\frac{1}{r} = \frac{1}{\sqrt{x^2+y^2}}$ as a result the reconstructed image by simple back-projection (Fig. 3-6) method is highly blurred and not the exact reconstruction.

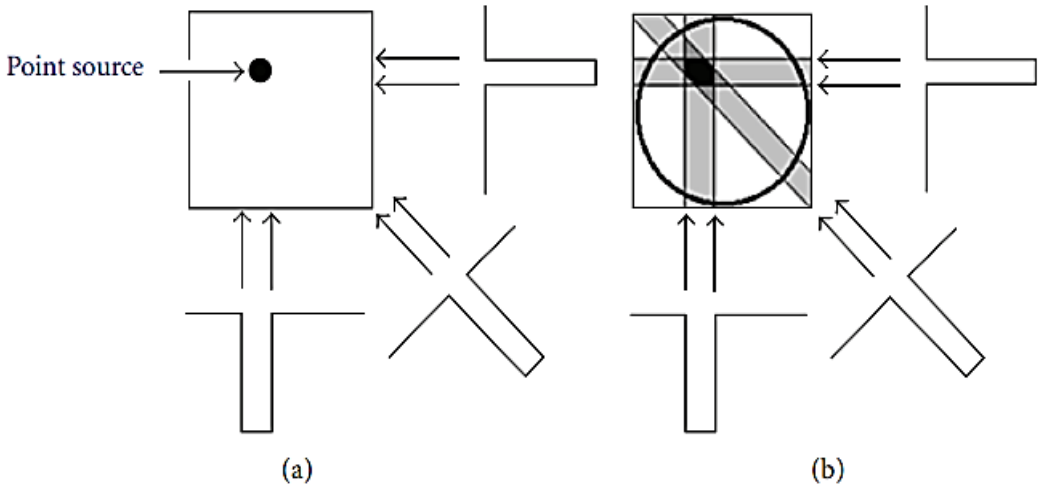

Figure 3-6: A simple representation of back projection (a) Acquisition of three projections. (b) Back-projected projections.

3.4.3 Filtered Back-Projection Method

The problem with simple back-projection is that it introduces blurring effect on the reconstructed image. Consequently, to alleviate this problem a filter can be applied before back-projection. Hence, the mechanism by which blurring effect is reduced by applying ramp filter on each sonogram and then back-project is known as filtered back-projection method (see Fig. 3-7). This is mathematically expressed as [28], [29]:

$$f(x,y) = \int_0^{\pi} \hat{P}_\theta(x')d\theta \tag{3.8}$$

where $\hat{P}_\theta(x')$ is the filtered version of $P_\theta(x')$ with the ramp filter which gives a weight proportional to its frequency to each of the components. The use of filter is to reduce amplitude of the low-frequency components of the sonogram and high frequency components around the edge are enhanced. Ramp filter is used so that both low and high frequency components are simultaneously reduced.

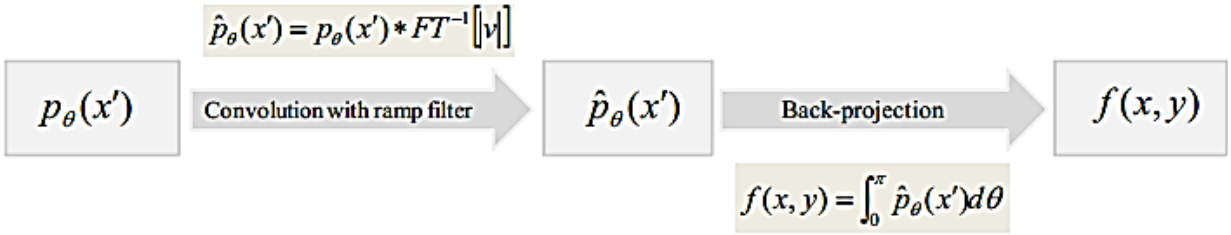

Figure 3-7: Flow of filtered back-projection (FBP) method.

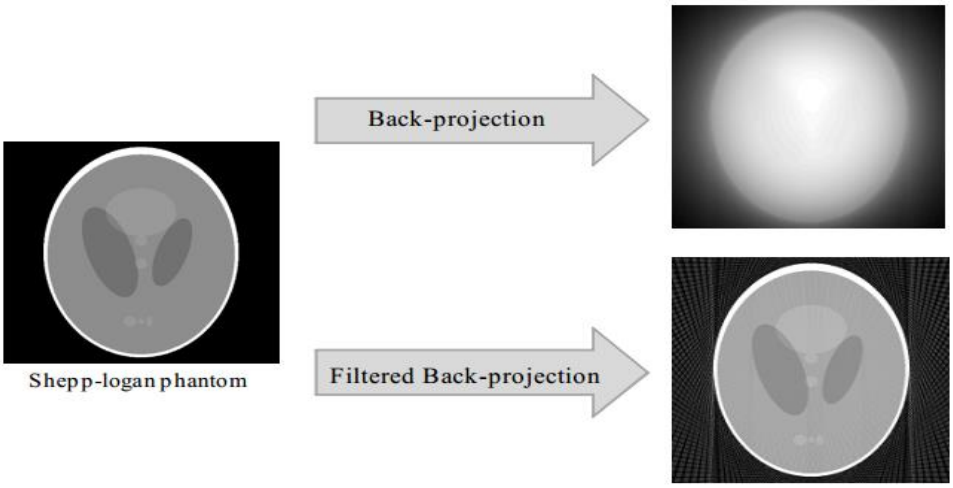

Figure 3-8: Comparative displaying of BP and FBP methods.

From Fig. 3-8 it can be seen that simple back-projection is very blurry and filtering before back-projection gives better result. In conclusion, analytical reconstruction methods work well when there are uniformly distributed large number of projections around the object otherwise it gives less satisfactory result when the number of projections is less than thirty six [29]. In the next section a better reconstruction technique, iterative reconstruction, will be discussed in detail.

3.5 Iterative Image Reconstruction

Because of modern and computationally powerful computers, iterative reconstruction (IR) method has become feasible in image reconstruction. As a result, traditional FBP reconstruction methods become obsolete. Currently emission tomography image reconstruction is often done using iterative reconstruction methods. The reason behind iterative reconstruction method popularity is that, it has improved image quality than analytic reconstruction, especially in terms of better signal to noise ratio (SNR). In addition, it takes into account both the effects of counting statistics and the physics of the measurements (e.g., scatter, normalization, and detector resolution). Moreover,

even if the number of projections is less, it gives a relatively better image reconstructed image [5], [23].

The concept behind iterative reconstruction is to reconstruct an image through successive iterative estimations (see Fig. 3-9). Iteration is commenced with an initial estimation of the image being reconstructed, which is often a uniform distribution initialized to 0 or 1. Following this, the next step is forward projection, i.e. image intensities along line of responses (LORs) are summed. Then, forward projected data is compared with the measured projection data. The difference between the measured and the forward projected data is then used to make adjustments to the previous image estimate along the measured LORs. The iteration process is repeated until estimated and measured projections are matched i.e. difference between the forward projected and measured data sets is minimized [6], [23], [28].

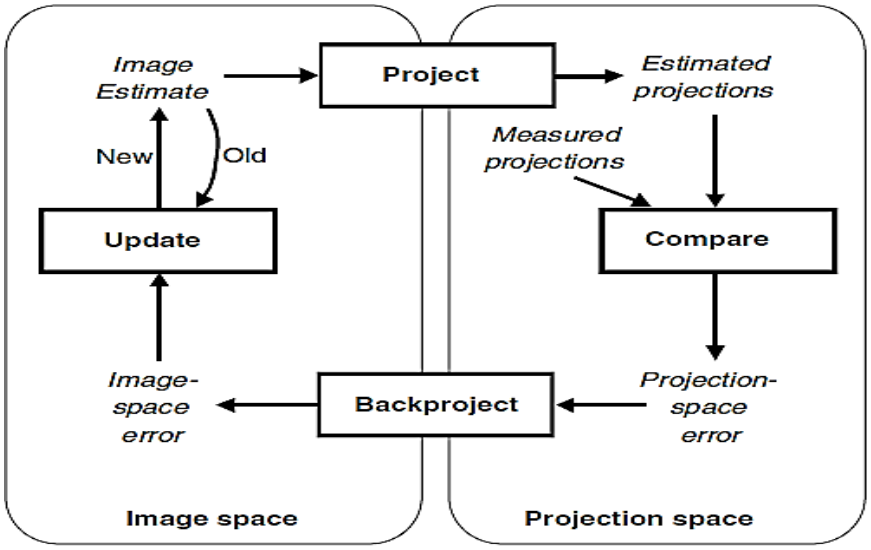

Figure 3-9: Flowchart of a generic iterative reconstruction algorithm.

3.5.1 Iterative Image Reconstruction Techniques

Iterative reconstruction is now a days a standard method of reconstruction in clinical use, resulting in improved image quality for emission tomography. Various iterative reconstruction methods have been developed, and of these methods, the most widely used reconstruction algorithm in emission tomography is the maximum likelihood expectation maximization algorithm (ML-EM) and its accelerated form based on ordered subsets (OS-EM) [16].

3.5.2 Algebraic Reconstruction Techniques

In an algebraic reconstruction technique (ART), an image to be reconstructed can be considered to be a linear system of equations (see Fig. 3-10), one for each projection bin [9], [33]. The main idea of the ART algorithm (which is also known as the Kaczmarz method) is to make the estimated image satisfy one equation at a time [34]. Its general model is shown in Fig. 3-12 and simple example is shown in Fig. 3-13.

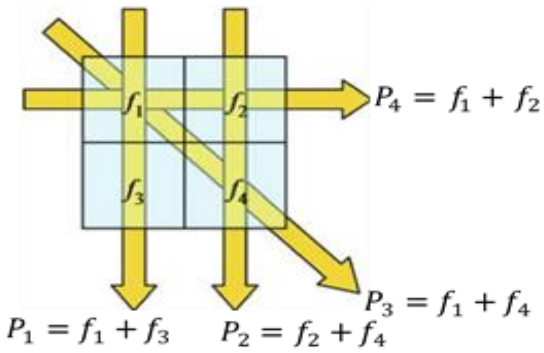

Figure 3-10: The principle of algebraic reconstruction is very simple. The set of projections results in a linear system of equations. All four unknown attenuation values can be determined exactly using four projections from three projection angles [34].

The mathematical formulation of the reconstruction problem is posed as a system of linear equations, which should be solved when reconstructing an image [28]:

$$\begin{aligned} A_{11}f_1 + A_{12}f_2 + A_{13}f_3 + \cdots A_{1N}f_N &= p_1 \\ A_{21}f_1 + A_{22}f_2 + A_{23}f_3 + \cdots A_{2N}f_N &= p_2 \\ \vdots \qquad \vdots \qquad \vdots \qquad \vdots & \\ A_{M1}f_1 + A_{M2}f_2 + A_{M3}f_3 + \cdots A_{MN}f_N &= p_M \end{aligned} \tag{4.1}$$

So we write the set of linear equations for each ray as:

$$\sum_{j=1}^{N} A_{ij}f_j = P_i, i = 1,2,\dots,M \tag{4.2}$$

where P_i is projection data along the i^{th} ray. In other words, the projection at a given angle is the sum of non-overlapping, equally wide rays covering the figure, M is the total number of rays (in all the projections). A_{ij} are the weights that represent the contribution of every pixel for all the

different rays in the projection. f_j are the values of all the pixels in the image and N is the total number of pixels in the image [28].

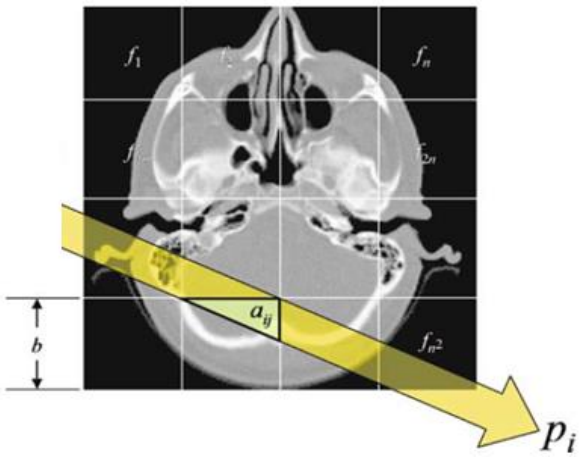

Figure 3-11: The γ-ray beam of width does not traverse all pixels of size b^2 equally when passing through the tissue. The area of the pixel section that has actually been passed through and that is to be reconstructed must be included in the system of equations as a weighting [28].

Assuming that this set of simultaneous equations is consistent (which occurs when there is no noise), the solution is any point that lies in the intersection of all the hyperplanes. This point can be determined by a process in which, starting from an initial estimate $f(0)$, the vector is repeatedly projected onto all the hyperplanes as illustrated in Fig. 3-11. The operation of projecting a point onto a hyperplane is a simple one, given in [26]:

$$\hat{f}_i^{(n+1)} = \hat{f}_i^{(n)} + h_{ji}\frac{\left(g_j - \sum_k h_{jk}\hat{f}_i^{(n)}\right)}{\sum_k h_{jk}^2} \tag{4.3}$$

The operation of projecting onto this set is simple. In each iteration, any pixel having a negative value is set to zero:

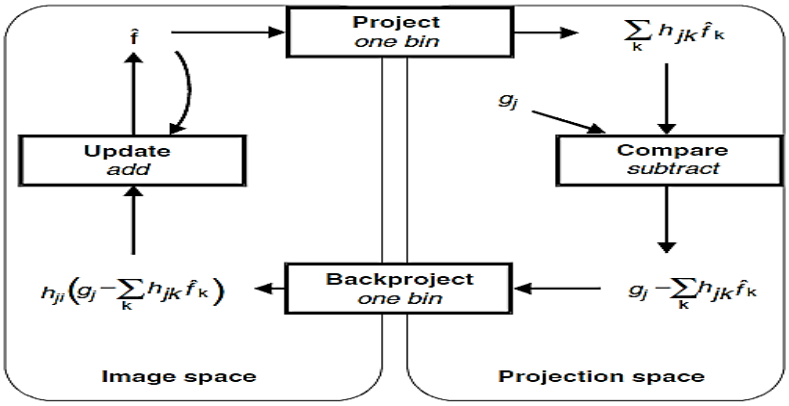

Figure 3-12: The algebraic reconstruction technique in the form of the general iterative model [26].

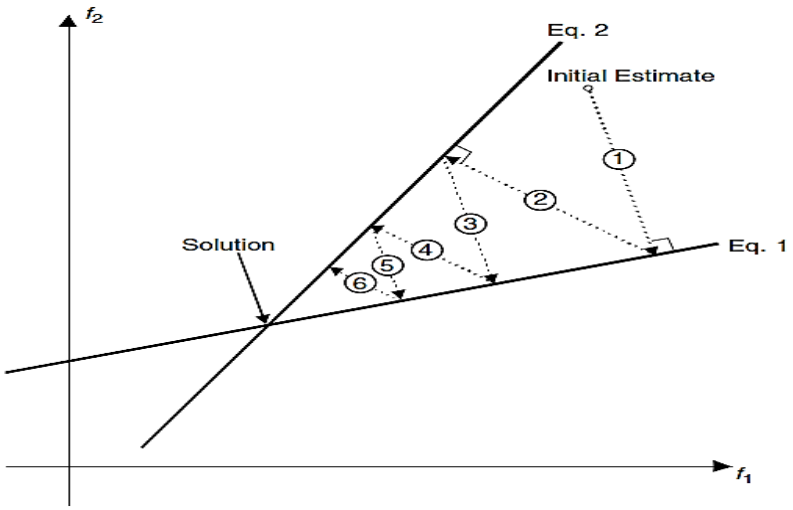

Figure 3-13: A simple example of the Kaczmarz procedure. The current estimate is projected successively onto each line by finding the point on each line that lies closest to the current estimate [26].

The convergence rate of the Kaczmarz/ART method may be dependent on the orthogonality of the successive equations. Note in Fig. 3-13 that when the equations are far from orthogonal, the process may require many iterations to reach the intersection. On the other hand, when the equations are more nearly orthogonal, the process requires relatively few iterations [1].

3.5.3 Statistical Reconstruction Techniques

Statistical reconstruction (SR) is now the preferred method of reconstruction. These algorithms calculate estimates of the likely distribution of annihilation events that led to the measured data, based on statistical principles, usually yielding improved noise profiles and resistance to the strip

artifacts common with FBP. The key reasons for using SPECT imaging equipment is that it corrects noise modeling and the ability to include a priori information in the image reconstruction objective function. In addition, it is considered superior when one does not have a large set of projections available and when the projections are not distributed uniformly in angle, or when the projections are sparse or missing at certain orientations [35]–[37].

3.5.3.1 Maximum-likelihood Expectation-maximization

Maximum-likelihood expectation-maximization (ML-EM) algorithm (and its modifications) is one of the frontend iterative reconstruction algorithms for SPECT image reconstruction [26]. The term Maximum Likelihood (ML) is used because the algorithm works by maximizing objective function i.e. likelihood function, which is the joint probability density function of Poisson random variables. When trying to maximize or minimize a likelihood function by taking partial derivatives with respect to all of its unknowns, these derivatives are set to zero. It turns out that Poisson likelihood function is too complicated for us to optimize. As a result the expected value (or the statistical mean value) of the likelihood function is calculated, which simplifies the problem. Thus the term Expectation "E". Then the maximum of the expected likelihood function is computed. Hence, Maximization "M". Consequently, we have the term Expectation-Maximization, "EM" [27].

In emission tomography (ET), a compound containing a radioactive isotope is introduced into the body and forms an unknown emitter density $\lambda(x, y)$ under the body's functional activity. Emissions then occur according to a Poisson process. The acquisition system usually consists of i detectors so that the measured data $y1, y2, \ldots, yi$ represents the counts of photons emitted by the body and measured by each one of the detectors [30].

The maximum likelihood expectation maximization algorithm (ML-EM) [5], [24], [25], [27] determines an estimate λ_j^{k+1} of λ_j^k which maximizes the probability $p(y_1, \ldots, y_2|\lambda_j^k)$ of observing the actual detector count data over all possible densities. Let $\boldsymbol{\lambda_j}$ represent the number of unobserved emissions in each of $\boldsymbol{j}$ boxes (pixels) partitioning an object containing an emitter and let $\boldsymbol{C_{ij}}$ be the probability of an emission in box $\boldsymbol{j}$ detected in the detector unit $\boldsymbol{i}$. ML-EM is an iterative reconstruction algorithm which starts with an initial estimate λ_0^0 and gives the new estimate λ_j^{k+1} from an old estimate λ_j^k. When applied to the ET reconstruction problem, the ML-EM framework

yields the following simple iterative equation, which is easy to implement and understand [26], [38]:

$$\hat{f}_i^{(n+1)} = \frac{\hat{f}_i^{(n)}}{\sum_{i'} h_{i'k}} + \sum_i h_{ij} \frac{g_i}{\sum_k h_{ik} \hat{f}_k^{(n)}} \tag{4.4}$$

This algorithm converges to the maximum likelihood estimate of a probability distribution function from the observed data. In this algorithm, the measured emission data is assumed a spatially dependent Poisson model [26], [38]. The general ML-EM iteration model is shown in Fig. 3-14.

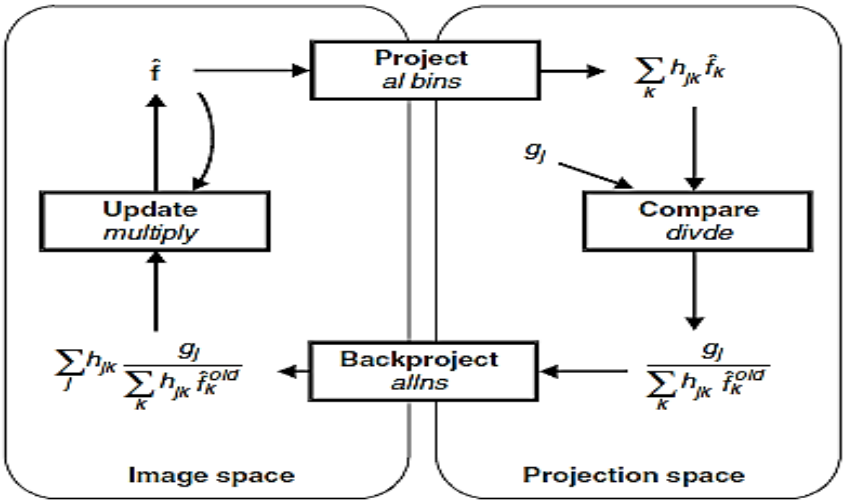

Figure 3-14: Maximum-likelihood expectation-maximization algorithm in the form of the general iterative model.

Although ML-EM algorithm gives good results for lower number of projections than FBP, it has two limitations. First, it has low convergence speed (i.e. it requires a higher number of iterations to yield usable solution) [26]. The reason is that each iteration requires one forward projection and one back-projection, which makes it one to two orders of magnitude more processing time than FBP. The second shortcoming is that as the iteration increases, it also starts to introduce more noise. Thus, in order to address these problems, several methods are proposed and one of the most widely used is ordered-subsets expectation maximization which is discussed in the section below [26], [27], [30].

3.5.3.2 Ordered Subset Expectation Maximization

Ordered subset expectation maximization (OS-EM) is the most widely used acceleration technique [39]. The OS-EM algorithm is a modification of the ML-EM algorithm [26]. The essential

difference between OS-EM and MLEM is the use of a subset of projections for updating rather than comparison of all estimated and measured projections [39]. In OS-EM reconstruction, the projection views are grouped in different sets (called subsets), selected in a specific order that attempts to maximize the new information being added in sub-iterations. Then the image is updated after each subset is considered. Fig. 3-15 shows an example of how the projection views are divided into subsets [27], [39].

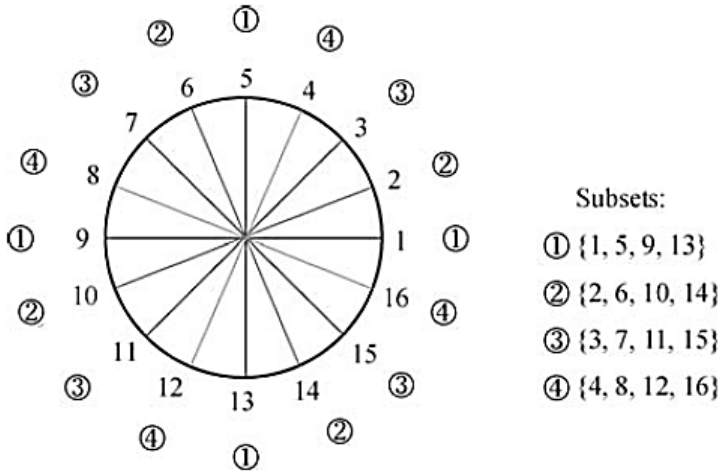

Figure 3-15: The total 16 projection views are divided into 4 subsets.

For OS-EM, one iteration is normally considered: the use of all data once; consequently use of only part of the data during the update process is termed a sub-iteration [39]. Further iterations may be performed by passing through the same ordered subsets, using as a starting point the reconstruction provided by the previous iteration [30]. Iteration proceeds by using different projections in each subsequent subset until all projections are used.

In OS-EM algorithm, increasing the number of subsets accelerates the convergence rate. However, the noise could also increase with number of subsets. Approximately speaking, if there are N subsets, the ML-EM algorithm accelerates about N times [27]. Nevertheless, when subset is reduced to a single subset encompassing all the projection data, the OS-EM algorithm reduces to the ML-EM algorithm [26]. The resulting equation is very similar to the standard ML-EM equation, the only difference being the use of subsets, S_n, where $n \epsilon N$, the total number of projections divided by the number of projections per subset or subset size [39]:

$$f_j^{new} = \frac{f_j^{old}}{\sum_{i \epsilon S_n} a_{ij}} \sum_{i \epsilon S_n} a_{ij} \frac{P_i}{\sum_k a_{ik} f_k^{old}} \quad (4.5)$$

Generally, one update in this algorithm is called a sub-iteration and one pass through all of the subsets is referred to as an iteration [26]. The sub-iterations recycle through S_n for subsequent iterations. The computation time for each sub-iteration is roughly equal to the time for a conventional ML-EM iteration divided by N, due to the reduced number of forward and back projection operations in the subset. Consequently, for 180 projections and subset size of 4, the acceleration factor is approximately 45 [39].

The great success of the OS-EM algorithm in speeding up the reconstruction process, along with improvements in computer power, has lessened the practical need for additional acceleration strategies. The organization of the subsets is important to the performance of the algorithm. In addition, mathematical difficulties can result if any subset does not contain some contribution from every pixel in the field of view; in this case, the first summation in the denominator of Eq. (4.5) is zero [26].

Form the literatures discussed in this chapter, we can observe that OS-EM subset ordering plays a great role in improving SPECT reconstruction accuracy and mainly reconstruction time. However, there are still rooms to improve the reconstruction accuracy as well as reconstruction time with the OS-EM method. That calls for the development of an improved version of the OS-EM, which is the subject of discussion in the next chapter.

Chapter 4 Methodology

This section deals with methodological issues of the proposed SPECT reconstruction scheme in the current thesis work including the SPECT geometrical setup, computing the **s**ystem probability matrix, calculation of common area, computing phantom projection, computing projection statistical measurements and sorting the system matrix.

4.1 SPECT Geometrical Setup

In the case of SPECT, the shape and dimensions of the collimator are the main geometrical parameters that have to be considered [40]–[42]. Typical SPECT geometrical parameters are stated in Table 4-1. Figure 4-1 shows the notation and coordinate system for SPECT imaging and reconstruction; λ_i is the value of the object radiation at the i-th pixel of object image and y_j is the measured radiation at the detector i.e. projection data at j-th bin, and P_{ij} is the system detection probability of photons emitted from pixel i that is being detected at detectors bin j.

Table 4-1: SPECT imaging simulation parameters.

Parameter	Dimension
Detector size	50 cm x 50 cm
Collimator diameter	1.409 mm
Gantry rotation radius	35 cm
Projection	32 x 32 matrix, 180 views over 360 degree
Pixel dimensions	4 x 4mm^2

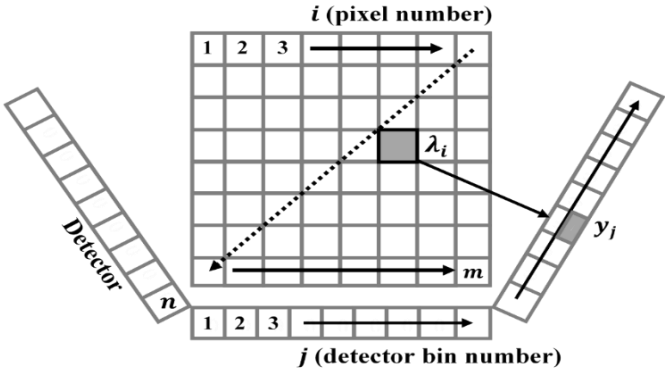

Figure 4-1: SPECT imaging system notation and coordinate systems

4.2 Computing the System Probability Matrix

The key element in iterative algorithms is the system probability matrix; a matrix that provides the probabilities with which each photon emitted from a pixel of the unknown image is detected. In this probability matrix, the geometrical setup of the system is taken into account [40]. The size of the probability matrix is often related to the dimension (2D/3D) of the acquisition, the number of detectors, the number of projection angles and the size of the reconstructed image. In typical applications, this matrix is very large and sparse (more than 95% of its elements are zeros) [40] and it is difficult to be stored or manipulated. Thus, when real-time calculation of the probabilities is required (e.g. in list mode reconstruction), analytical geometrical methods have to be used. In this thesis analytical geometrical calculation is used to compute the system probability matrix [40].

Theoretically, all counts emitted from a pixel i should be detected from all detectors j. However, this does not happen due to a number of reasons such as scattering, attenuation, detector dead areas (i.e. detectors collimator), etc. Since non-detected counts cannot be included in the reconstruction process, the P_{ij} elements are limited to those that are actually detected from the detectors [40]:

$$P_{ij} = \frac{photons\_emitted\_from\_pixel\_i\_detected\_from\_detector\_j}{photons\_emitted\_from\_pixel\_i\_totally\_detected} \tag{4.1}$$

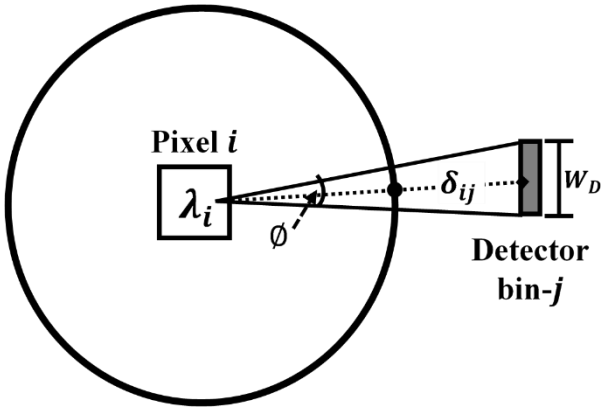

Figure 4-2: The geometry of photons emission from pixel i that are detected at detector j.

Assuming that: (i) photons are emitted isotropically from each pixel; (ii) each photon is following a linear orbit, the following parameters are defined:

- λ, pixel emission rate (photons/s)
- E, pixel area;
- T, acquisition time;
- δij, distance between pixel i and detector j;
- W_D, the width of each detector;
- D, the distance from the center of rotation.

As it can be seen in Fig. 4-2, if a photon is emitted form pixel i, the probability that it will be detected from detector j (in this case the detector "sees" 100% of pixel area) is:

$$\frac{P'_{ij}}{P_{o\lambda}} = \frac{\phi}{2\pi} \overset{P_{o\lambda}=1}{\Longrightarrow} P'_{ij} = \frac{\phi}{2\pi} \tag{4.2}$$

Angle ϕ is given by:

$$\phi = 2arctan\left(\frac{W_D}{2\delta_{ij}}\right) \tag{4.3}$$

From Eq. (4.2) and Eq. (4.3), it can be derived:

$$P'_{ij} = \frac{arctan\left(\frac{W_D}{2\delta_{ij}}\right)}{\pi} \tag{4.4}$$

Assuming the center of rotation is the point with coordinates (0,0), δ_{ij} is given form:

$$\delta_{ij} = \sqrt{\left(x_i - x_j\right)^2 + \left(y_i - y_j\right)^2} \tag{4.5}$$

where (x_i, y_i) is the coordinates of (the center of) pixel i and $\left(x_j, y_j\right)$ the coordinates of (the center of) detector j.

4.3 Calculation of Common Area

In order to calculate the common (overlapped) area, $E_{\%ij}$ (see Fig. 4-3) the area between detection zones (i.e. between projection lines of the detector bin) touching each pixel, coordinate geometry is used. The common area is a polygon i.e. an area enclosed by multiple straight lines, with a

minimum of three straight lines, called a triangle, to a limitless maximum of straight lines. A mathematical algorithm known as shoelace algorithm (also known as Gauss's area formula and the surveyor's formula) [26] is used to compute the area of a simple polygon whose vertices are described by their Cartesian coordinates in the plane [23]. Corresponding coordinates are cross-multiplied to find the area encompassing the polygon, and subtract it from the surrounding polygon to find the area of the polygon within.

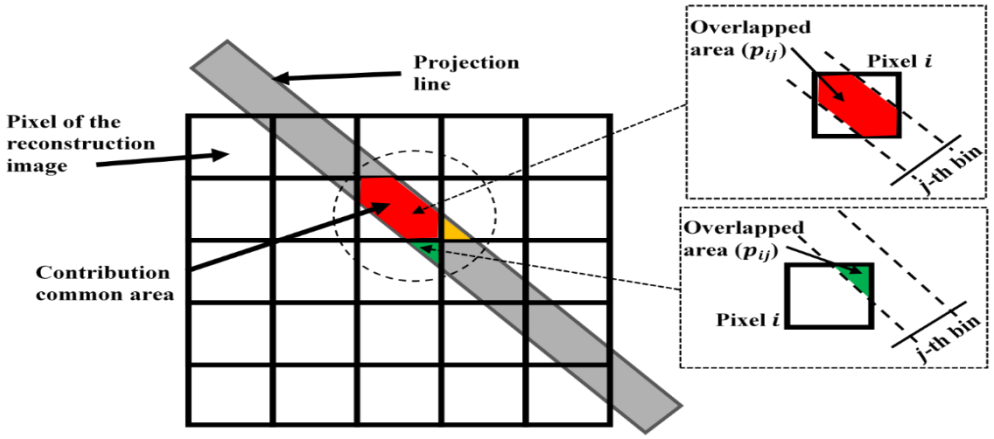

Figure 4-3: A 2D presentation of the relationship between a projection line and the reconstructed lattice. The different colors in the circle show the common areas in the selected region of the lattice. The colors represent the different elements of the system matrix.

During the time of scanning, when the SPECT gamma camera rotates around the object, we get different types geometrical shapes. Generally these shapes are polygons, so by using polygonal area formula we can calculate the common area. First step in computing the polygonal area is to number the vertices in order, going either clockwise or counter-clockwise, starting at any vertex. All possible regions of cross sectional areas are shown in Fig. 4-4.

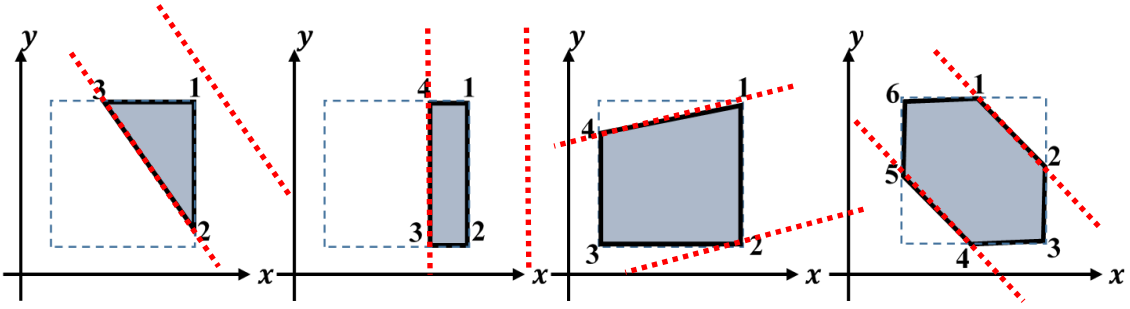

Figure 4-4: Common geometry shapes in the detection zone of photons emission for different angle of projection.

The area formula for any polygon is given by:

$$E = \left| \frac{(x_1 y_2 - y_1 x_2) + (x_2 y_3 - y_2 x_3) \ldots + (x_n y_1 - y_n x_1)}{2} \right| \tag{4.6}$$

where x_n is the x coordinate of vertex n and y_n is the y coordinate of n'th vertex. As seen in Eq. (4.6), the expression wraps around back to the first vertex again.

The total number of detected photons is:

$$\lambda T E_{\%} P'_{ij} \tag{4.7}$$

where $E_{\%}$ is the percentage of the area of intersection of pixel i and the "detection zone" of detector j. Finally, we get:

$$P_{ij} = \frac{\lambda T E_{\%} P'_{ij}}{\lambda T E_{\%i1} P'_{i1} + \cdots + \lambda T E_{\%iD} P'_{iD}} \Rightarrow P_{ij} = \frac{E_{\%} P'_{ij}}{\sum_{j=1}^{D} E_{\%ij} P'_{ij}} \tag{4.8}$$

where the product $E_{\%} P'_{ij}$ equals the probability that a photon emitted from pixel i is detected from detector j. Thus, the calculation probability P_{ij} requires the calculation of the common area $E_{\%ij}$.

4.4 Computing the Phantom Projection

Phantom projection at element j, P_j is computed using the formula:

$$P_j = \sum_{i=1}^{B} \lambda_i P_{ij} \tag{4.9}$$

where $\lambda_i = \{\lambda_1, \lambda_2, \lambda_3 \ldots, \lambda_B\}$ are pixel values and P_{ij} is the system matrix.

Similarly, back-projection of pixel i, x_i is computed as:

$$x_i = \sum_{j=1}^{D} d_j y'_j \tag{4.10}$$

where D is the total number of detectors, d_j is total counts at detector element j and $y'_j = \frac{P_{ij}}{P_j}$.

4.5 Compute Projection Statistical Measurement

In order to find part of the projections with a lot of information to get a better reconstruction accuracy, statistical measurements such as variance (σ^2), standard deviation (σ) and entropy are used. Variance and standard deviation measures of dispersion provide information on the spread of the data around the center. Consequently, projection with a high variance or dispersion is the part of projection with more information to accelerate image reconstruction. For projection sets $\{P_1, P_2, P_3 \dots P_n\}$ where n is the total number of projections with mean $\bar{P} = \frac{1}{n}\sum_{i=1}^{n} P_i$, the equations for variance, standard deviation and entropy are given in Eq. (4.11), Eq. (4.12) and Eq. (4.13) respectively:

$$Variance\ (P_1, P_2, P_3 \dots P_n) = \frac{1}{n}\sum_{i=1}^{n}(P_i - \bar{P})^2 \tag{4.11}$$

$$\text{Standard deviation}\ (P_1, P_2, P_3 \dots P_n) = \sqrt{\frac{\sum_{i=1}^{n}(P_i - \bar{P})^2}{n}} \tag{4.12}$$

$$Entropy\ (P_1, P_2, P_3 \dots P_n) = -\sum_{i=1}^{n} P_i \log P_i \tag{4.13}$$

4.6 Sorting the System Matrix

Based on the statistical measurements, the system matrix is reordered in descending order so that projection with more information is used early in the image reconstruction. As a result, the reconstruction accuracy is enhanced quicker.

4.7 The OS-EM Algorithm

As mentioned in the previous chapter, OS-EM is modification of the ML-EM algorithm which can be described as follows:

$$\lambda_i^{k+1} = \frac{\lambda_i^k}{\sum_{j=1}^{D} P_{ij}} \sum_{j=1}^{D} \frac{d_j P_{ij}}{\sum_{i=1}^{B} \lambda_i^k P_{ij}} \tag{4.14}$$

where:

- Image size: $N \times N \rightarrow 1 \times B, B = N^2$
- Image element (b): $i = 1, 2, 3, \dots, B$
- λ: Unknown activity distribution
- k: Is the iteration number
- i: Pixel location on object
- λ_i^k: Value of pixel at i and k
- d_j: Total counts at detector element j
- P_{ij}: Probability of λ_i photon detected, emitted from pixel i and detected from detector j at a given angle
- A: No of projection angles
- M: No of projection elements
- A sinogram size: $A \times M \rightarrow 1 \times D,\ D = AM$
- Detector element (d): $j = 1, 2, 3, \dots, D$

Now the OS-EM algorithm is given by:

$$\lambda_i^{k+1} = \frac{\lambda_i^k}{\sum_{j' \epsilon S_n} P_{ij}} \sum_{j' \epsilon S_n} P_{ij} \frac{d_j}{\sum_{i=1}^{B} \lambda_i^k P_{ij}} \tag{4.15}$$

where S_n is a subset. The flow chart is shown in Fig. 4-5.

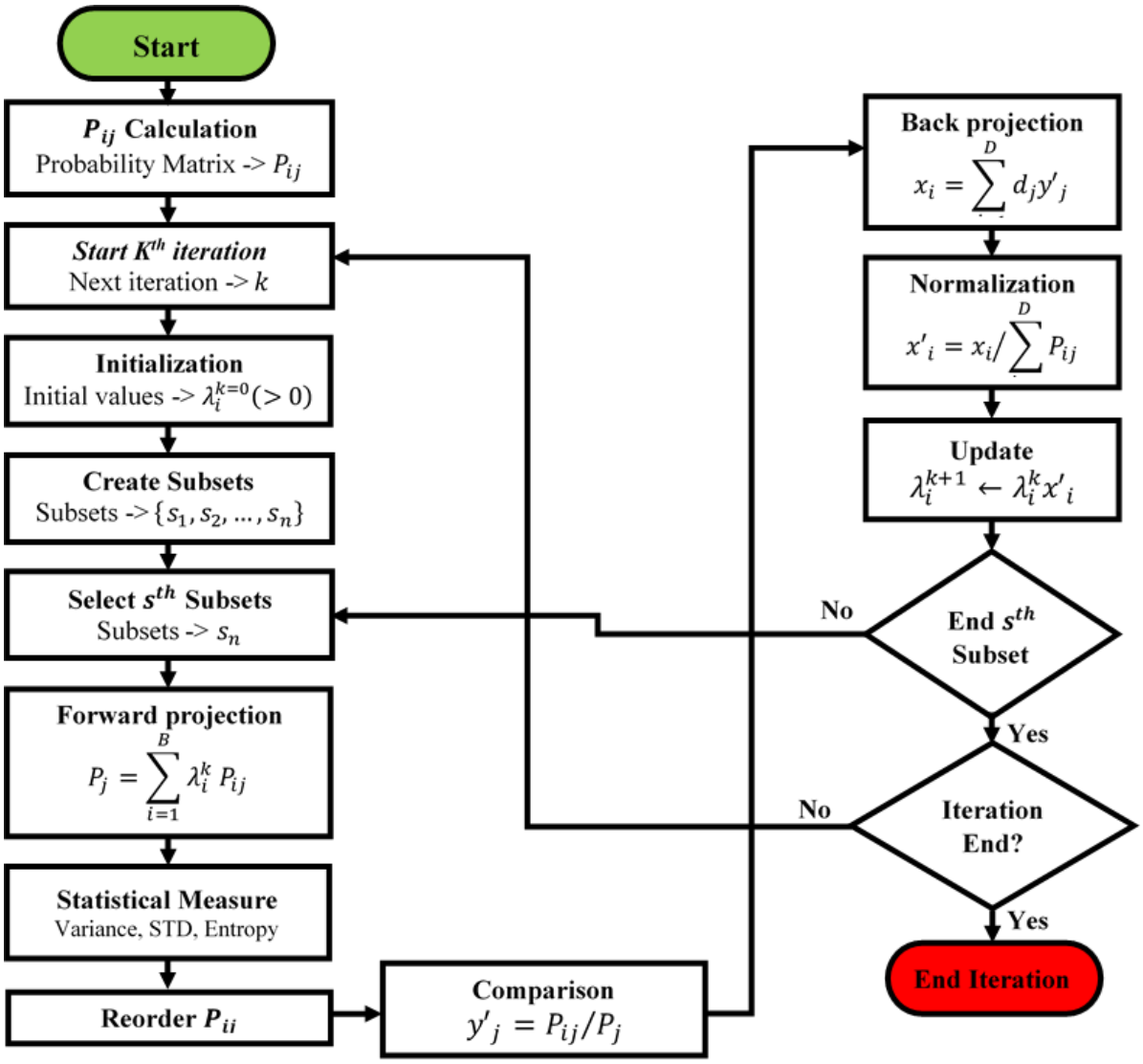

Figure 4-5: The OS-EM iterative reconstruction flow chart.

Chapter 5 Results and Discussion

5.1 SPECT Simulation Model Geometry

SPECT imaging geometry for different projection angles is shown in Fig. 5-1, 180 projection angles with 2° step angle were acquired over 360° rotation. As it can be seen in the figure, the rotation radius is $35cm$ and the imaging subject is assumed to be $50 \times 50\ cm^2$. Moreover, the detector width of $50cm$ with 32 detectors was assumed. Based on the simulation, 180 projections were acquired to be reconstructed into 32×32 image frames**. (a)**

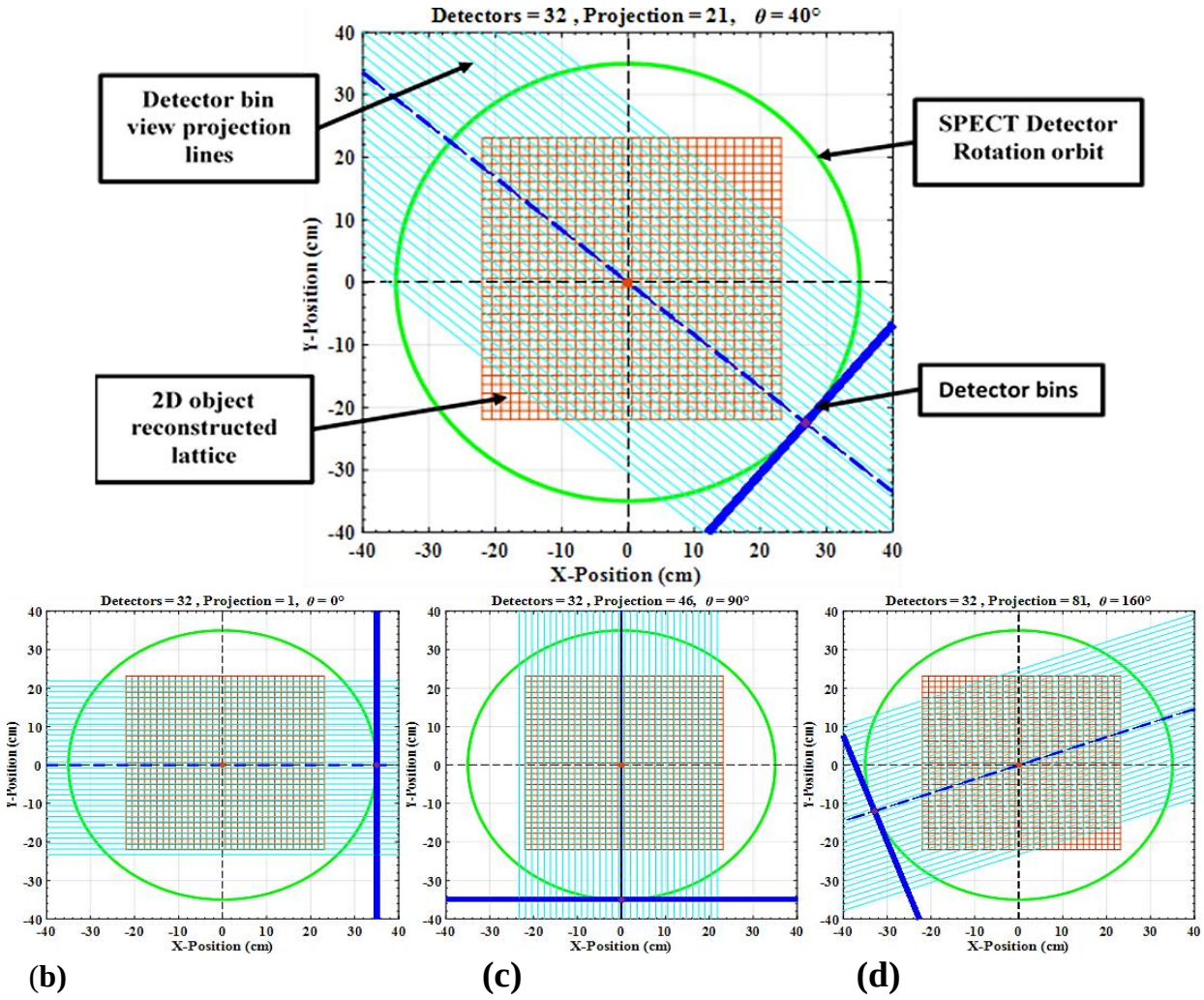

Figure 5-1: SPECT imaging geometry simulation for different projection angles Ø= 40°,0°,90°,160° (a), (b), (c), (d) respectively.

5.2 Find Detection Zone Pixel Intersection Points

In order to calculate the overlap area $(E_{\%ij})$ of the detection zone, first each intersection point of every pixel with the detection zone projection line must be computed. As it can be seen in Fig. 5-2, the point with blue mark 'x' is intersection of projection line with the pixel horizontal line and the point with green mark 'y' is intersection point of projection line with the pixel vertical line. Following this and adding the corner points if any as a vertex for the region of interest, geometry coordinate system Eq. (5.6) is used to calculate the overlap area.

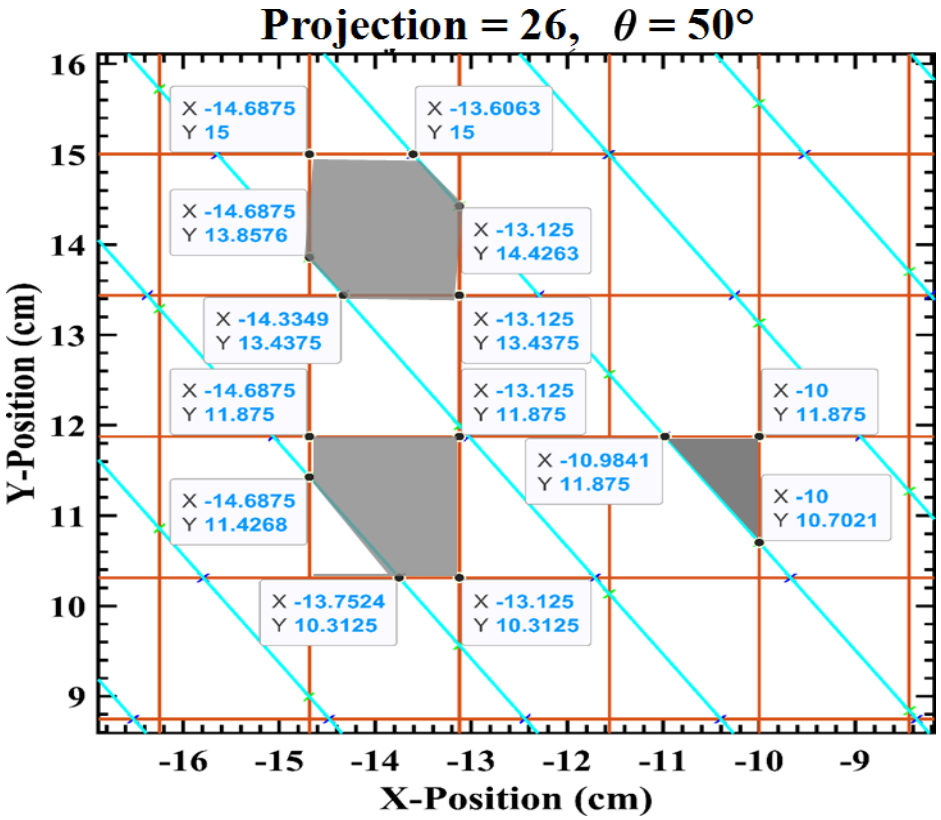

Figure 5-2: Common areas in the selected region of the lattice for an angle of projection 50°.

5.3 Calculating Distance from Pixel Center to Detector

Calculating the distance $(\boldsymbol{\delta_{ij}})$ from the center of the pixel to the detector is important to model the contribution of each pixel in each detector. Pixels near to the detector contribute more energy on the detector than pixels further to the detector. Figure 5-3 shows how the distance is measured. Now photons emitted from pixel $\boldsymbol{i}$ detected from detector can be calculated using Eq. (5.4)

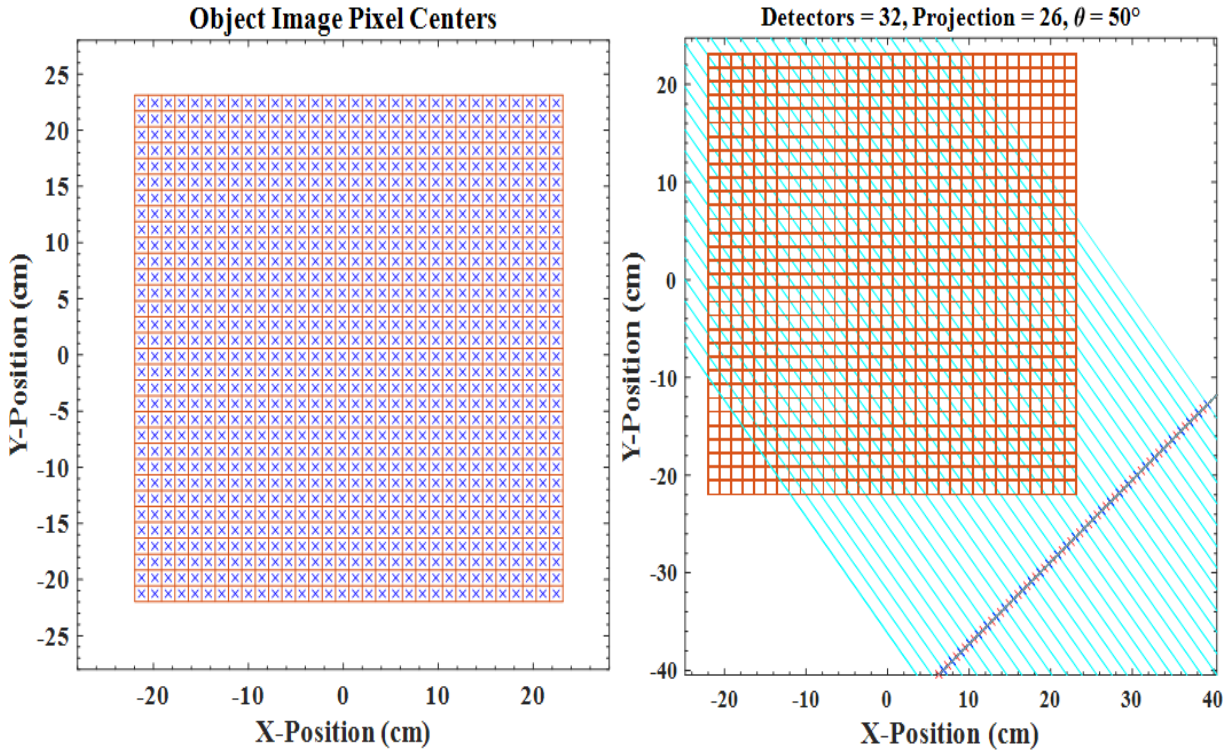

Figure 5-3: Calculation of distance of pixel center to detector (a) Pixel centers (b) Sample distance of pixel center to center of detector bin for 26th projection at angle 5o°.

5.4 System Probability Matrix

System probability matrix is a matrix containing the information of each object pixel contribution on the SPECT detector. As shown in Fig. 5-4 the horizontal axis is the total number of detectors i.e. the product of total number of projection and total number of detectors which is $180 \times 32 = 5760$. On the other hand the vertical axis shows the number of pixels i.e. $32 \times 32 = 1024$. If the pixel is closer and more aligned with the detector, it will have higher probability to contribute on the detector otherwise if the pixel is further from the detector or misaligned with the detector, the contribution probability is low.

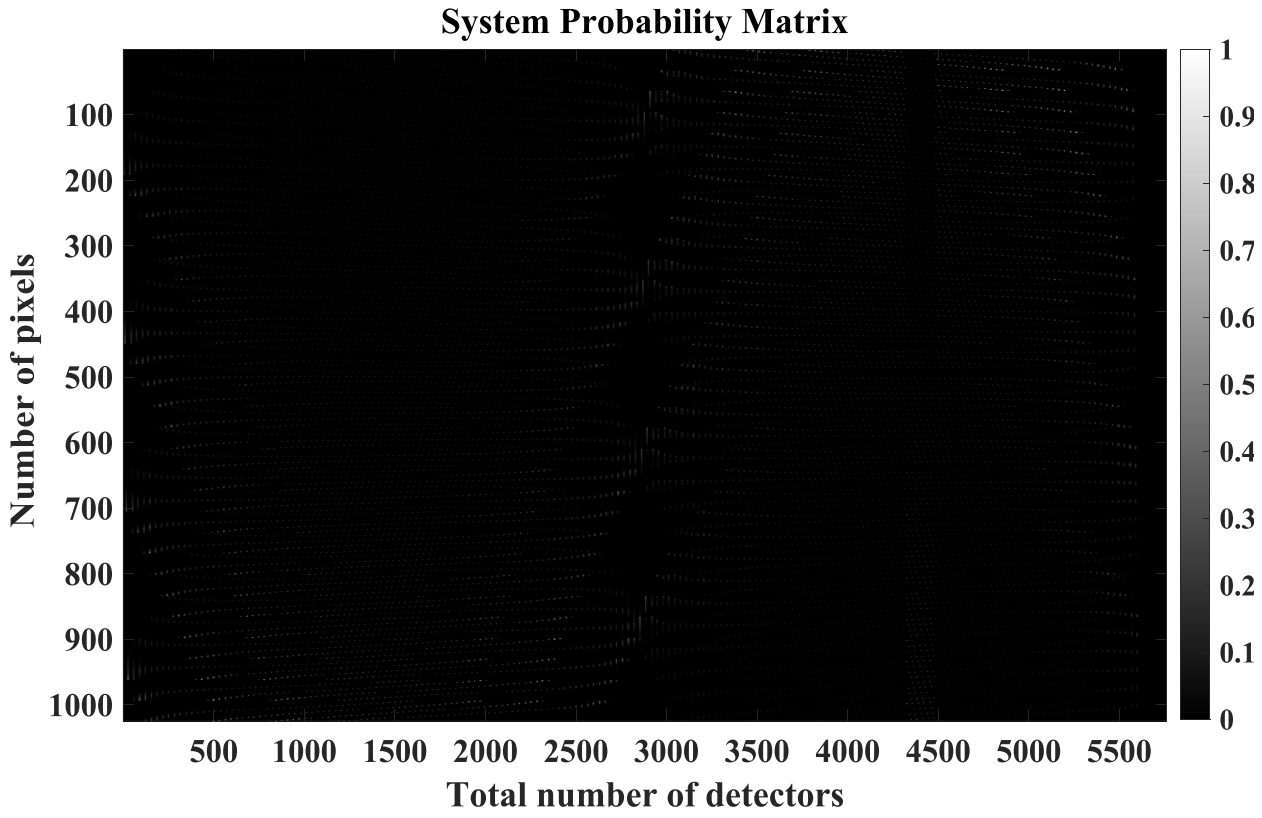

Figure 5-4: System probability matrix: the horizontal axis is the total number of detectors (number of projections x number of bins in the detector crystal = 180×32=5760) and the vertical axis is number of pixels i.e. 32×32=1024.

5.5 Phantom Projections

Commonly used phantoms to perform SPECT image reconstruction are Shepp-Logan, Jaszczk, and Thorax phantom. In this thesis, these phantoms are used to check the performance of the proposed reconstruction scheme. Figure 5-5 presents projections of the three phantoms. The forward projection was done using Eq. (4.9). The number of projections is 180 over the 360° angle, i.e. with 2° step angle of projection.

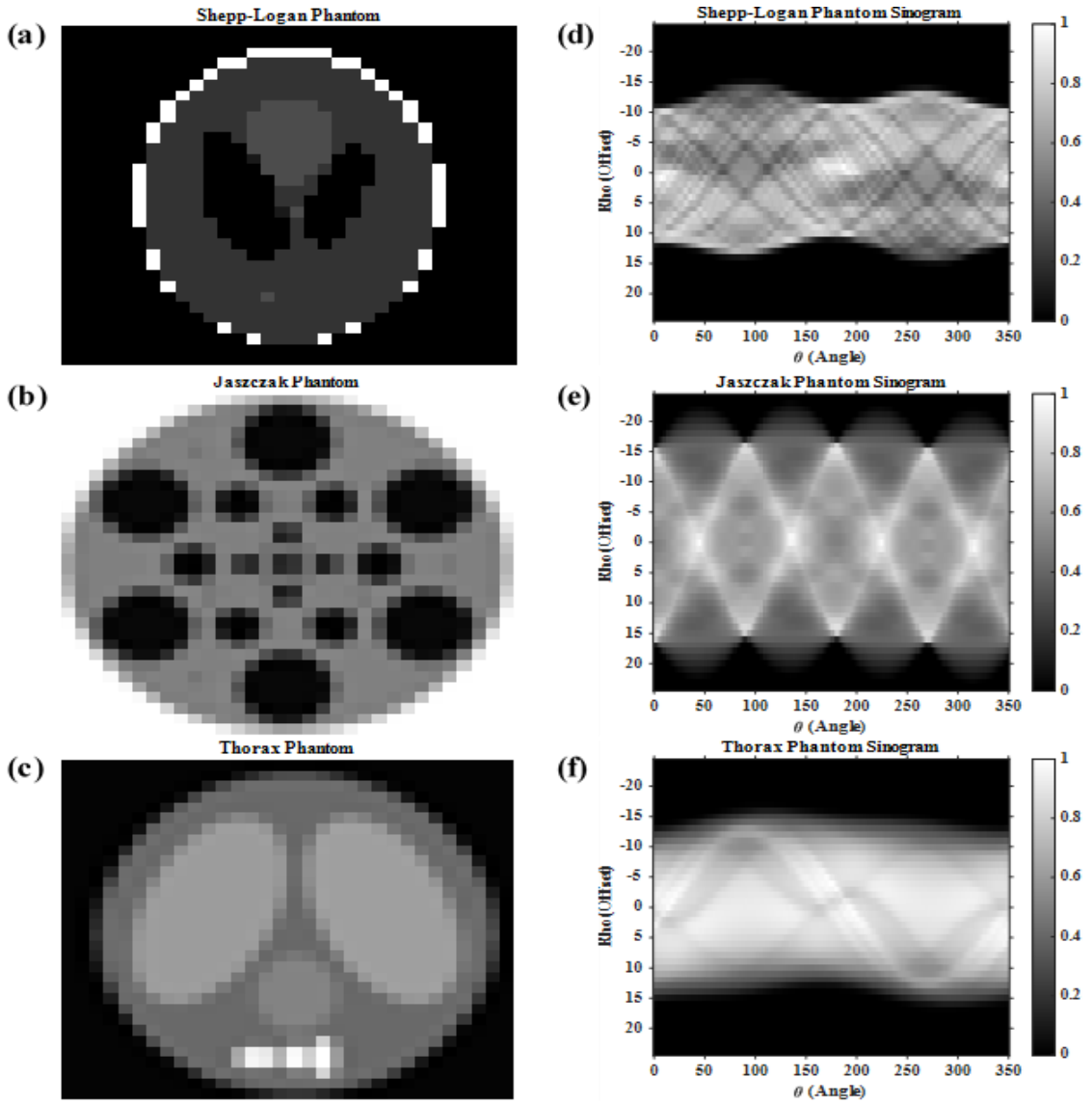

Figure 5-5: Three phantoms (left column) and their projections (right column).

5.6 Projection Statistical Measure

Figure 5.6 presents projections of the three phantoms used in this study and statistical measures (variance and entropy) derived from them. From the figure one can observe that projection statistical measure with higher variance has more information. Use of projections with higher information during image reconstruction dramatically improves the accuracy of the reconstruction and makes the algorithm more resistant to noise as the number of iterations increases, which implies a more stable algorithm.

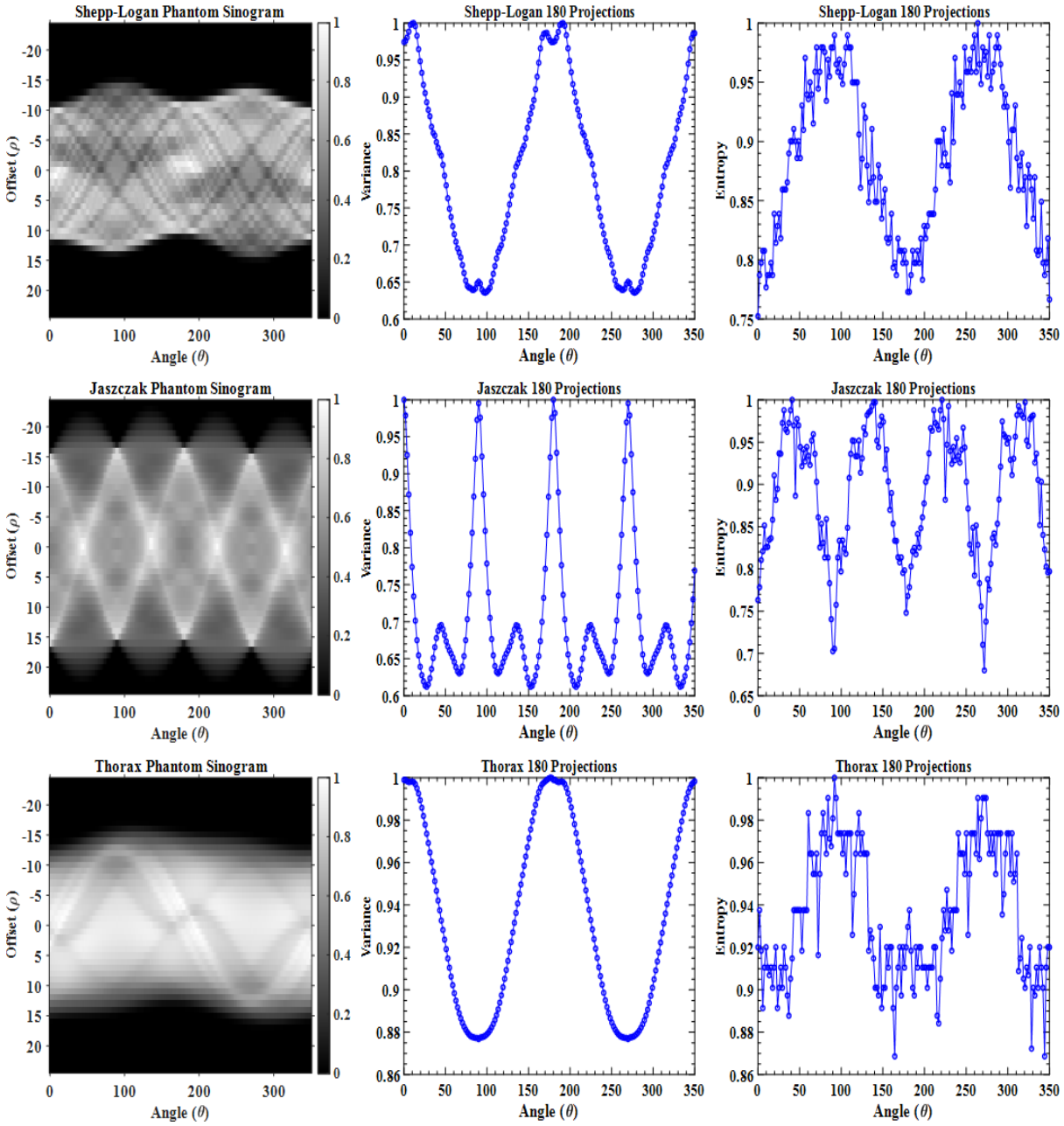

Figure 5-6: Phantoms and their statistical measures for 180 projection angles: Phantoms (left column), variance statistical measurement (middle column) and entropy statistical measurement (right column).

5.7 SMS-OSEM Reconstruction Iteration Progress

Following the computation of statistical measures and applying the ordered subset based on statistical measures on the OS-EM reconstruction algorithm, phantoms are reconstructed. It can be seen in Fig. 5-7 that as the number of iteration increases, the similarity accuracy also increases

after first iteration. Moreover, comparing the three reconstructions (OS-EM without modification, OS-EM based on variance and OS-EM entropy based) it is observed that variance based OS-EM reconstruction results in better accuracy and noise resistance (more stable). The reconstruction progress for Jaszczak and Thorax phantoms is presented in Appendix A and Appendix B respectively.

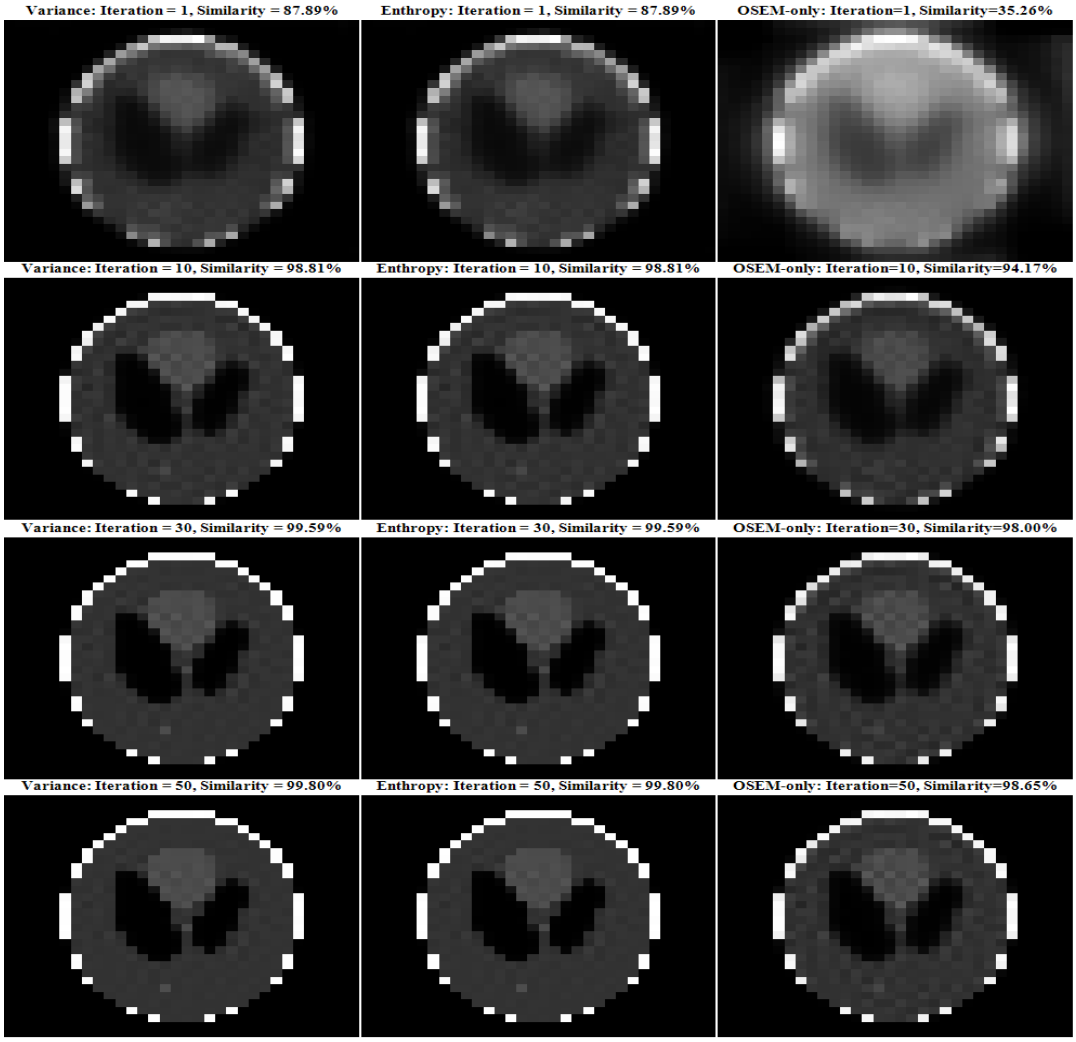

Figure 5-7: Shepp-Logan reconstruction progress: without OS-EM modification (left), variance based OS-EM (middle) and entropy based OS-EM (right).

5.8 Number of Subsets, Time and Similarity Relation in SMS-OSEM Reconstruction

In order to choose the best number of subsets, reconstruction analysis was made for different number of iterations. Then the number of subsets with lowest reconstruction time is selected. The results indicate that as the number of subsets increases, reconstruction time starts decreasing and increasing again. This is shown on Fig. 5-8. In addition, it is observed that the reconstruction time depends not only on the number of subsets but also on the type of phantom used. The right-column of Fig. 5-8 shows that as the subsets increase, the similarity also increases. With the number of subsets getting higher and higher, and particularly for some iterations, the SMS-OSEM algorithm could be unstable forcing the time to pick up again and the similarity starts decreasing abruptly. For instance, in Shepp-Logan phantom and Thorax phantom, for various iterations the algorithm breaks when the number of subsets is 15 and 30 respectively. For Jaszczak phantom the algorithm breaks when the number of subsets is 45. Thus, for Shepp-Logan, Jaszczak and Thorax the number of subsets could be optimally chosen to be at 15, 45, and 30 respectively. The choice also guarantees minimum reconstruction time for the three phantoms as can be seen on Fig. 5-8. .

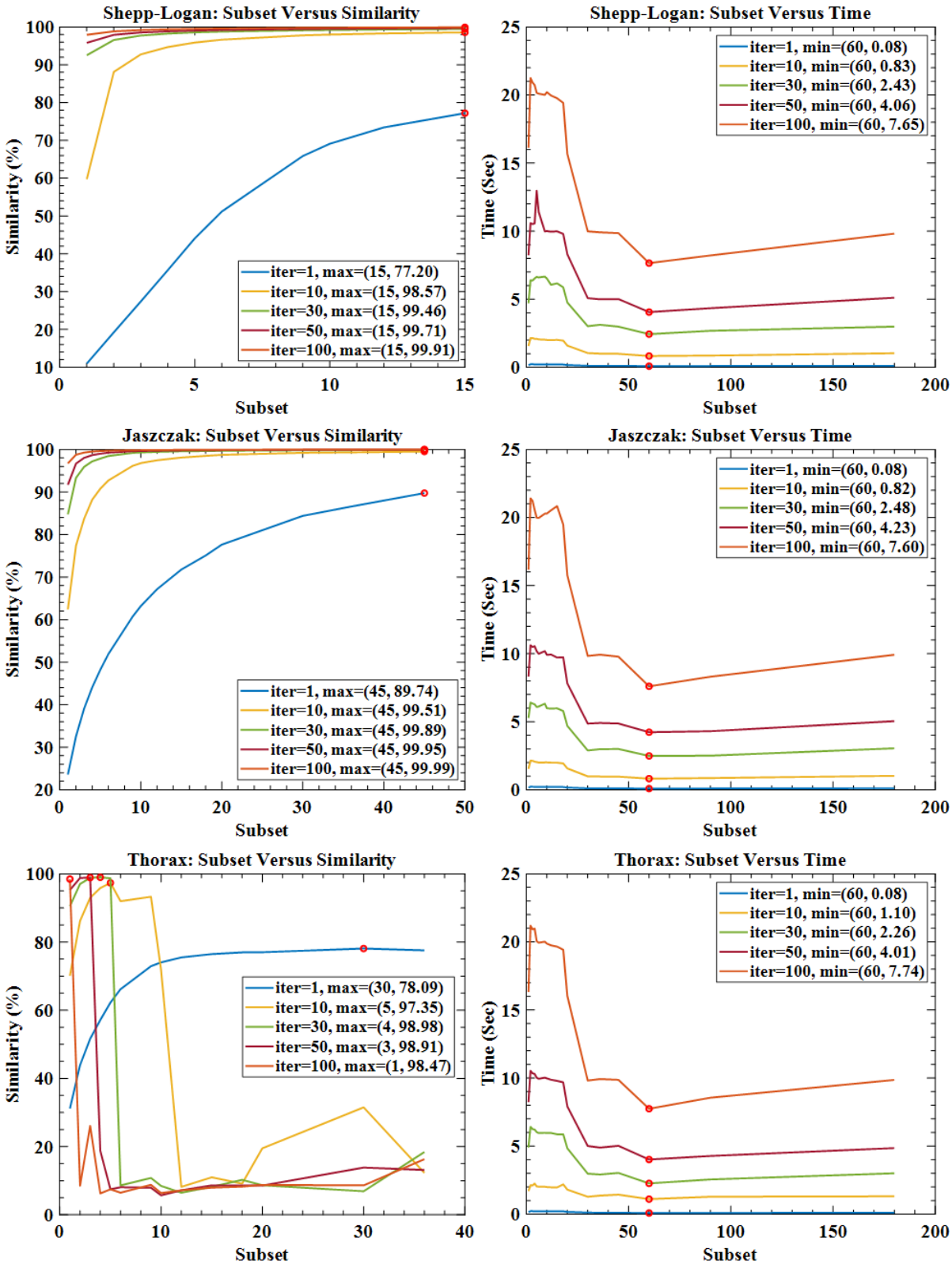

Figure 5-8: Relation between number of subsets with time of reconstruction, similarity and iteration. Subset versus similarity (left-column) and Subset versus time (right-column).

5.9 Phantom Reconstruction Comparison

The main phantom types used in SPECT reconstruction are shown in Fig. 5-9. From the figure it can be observed that different phantoms need different number of iterations to reach peak accuracy. In addition, as the number of iterations increases, both variance based and entropy based OS-EM reconstruction outputs become similar. For instance both Shepp-Logan and Jaszczak phantom require 100 iterations before reaching peak similarity and at this stage variance based and entropy based reconstruction similarities are more or less equal. However, for the Thorax phantom, it requires 30 iterations for variance based and 18 iterations for entropy based reconstructions to reach peak similarity. Hence it implies that statistically modified subset OS-EM (SMS-OSEM) reconstruction accuracy depends on the image being observed and further research can be done how the quality of the phantom affects the reconstruction.

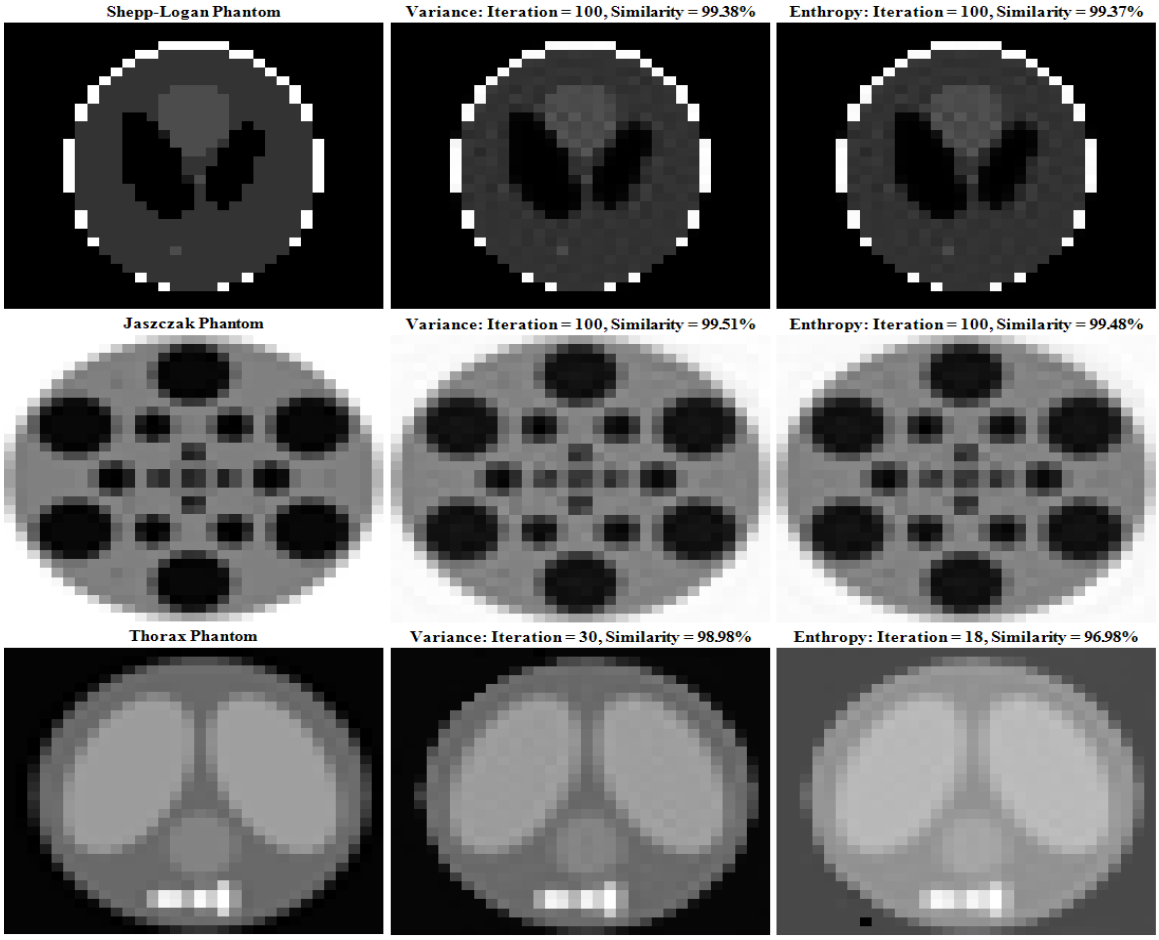

Figure 5-9: Phantom SMS-OSEM reconstruction. Original phantoms (left), variance based OSEM reconstruction (middle) and entropy based OSEM (right).

5.10 Performance of SMS-OSEM Reconstruction

After choosing the best number of subsets for the specific phantom used, comparison was made between the SMS-OSEM based reconstruction and ordinary OSEM reconstruction (i.e. without modification) and the results are shown in Fig. 5-10. From the figure, it can be deduced that variance and standard deviation based subset OSEM modifications achieved high accuracy quicker than ordinary OSEM and entropy. In addition, it also offered relatively more stable reconstruction, i.e. more resistive to noise as the number of iterations increase. Nevertheless, it is noted that in reconstruction of the Thorax phantom, ordinary OSEM became more resistive to iteration increment noise.

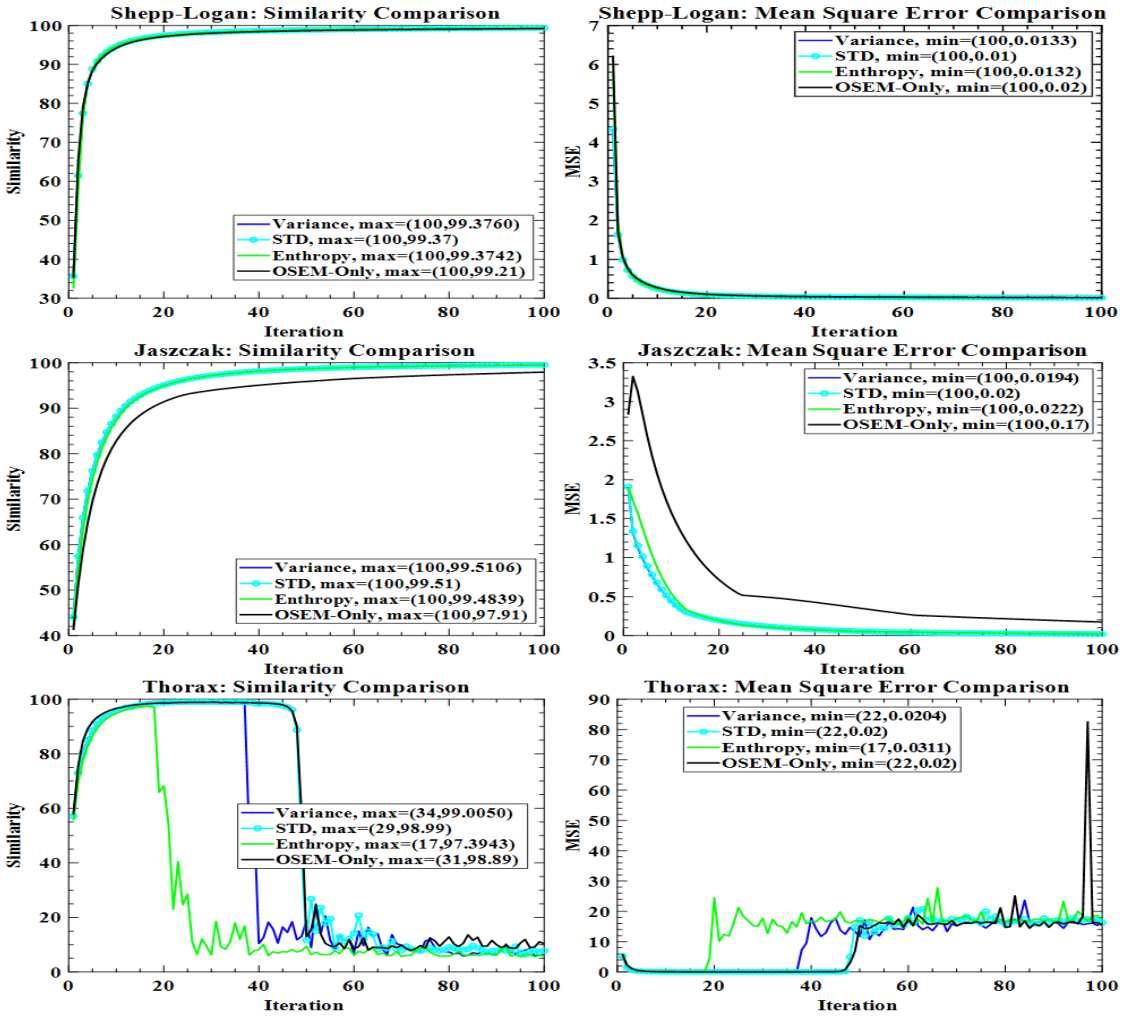

Figure 5-10: SMS-OSEM versus ordinary OSEM for phantoms 1-3 (rows 1-3 respectively): Similarity comparison (left-column) and mean square error comparison (right-column).

Moreover, reconstruction for Jaszczak had a wide accuracy difference compared to Shepp-logan phantom and Thorax phantom. This means that the phantom structure affects the reconstruction process. Overall, SMS-OSEM reconstruction offered better accuracy with less reconstruction. time than ordinary OSEM reconstruction.

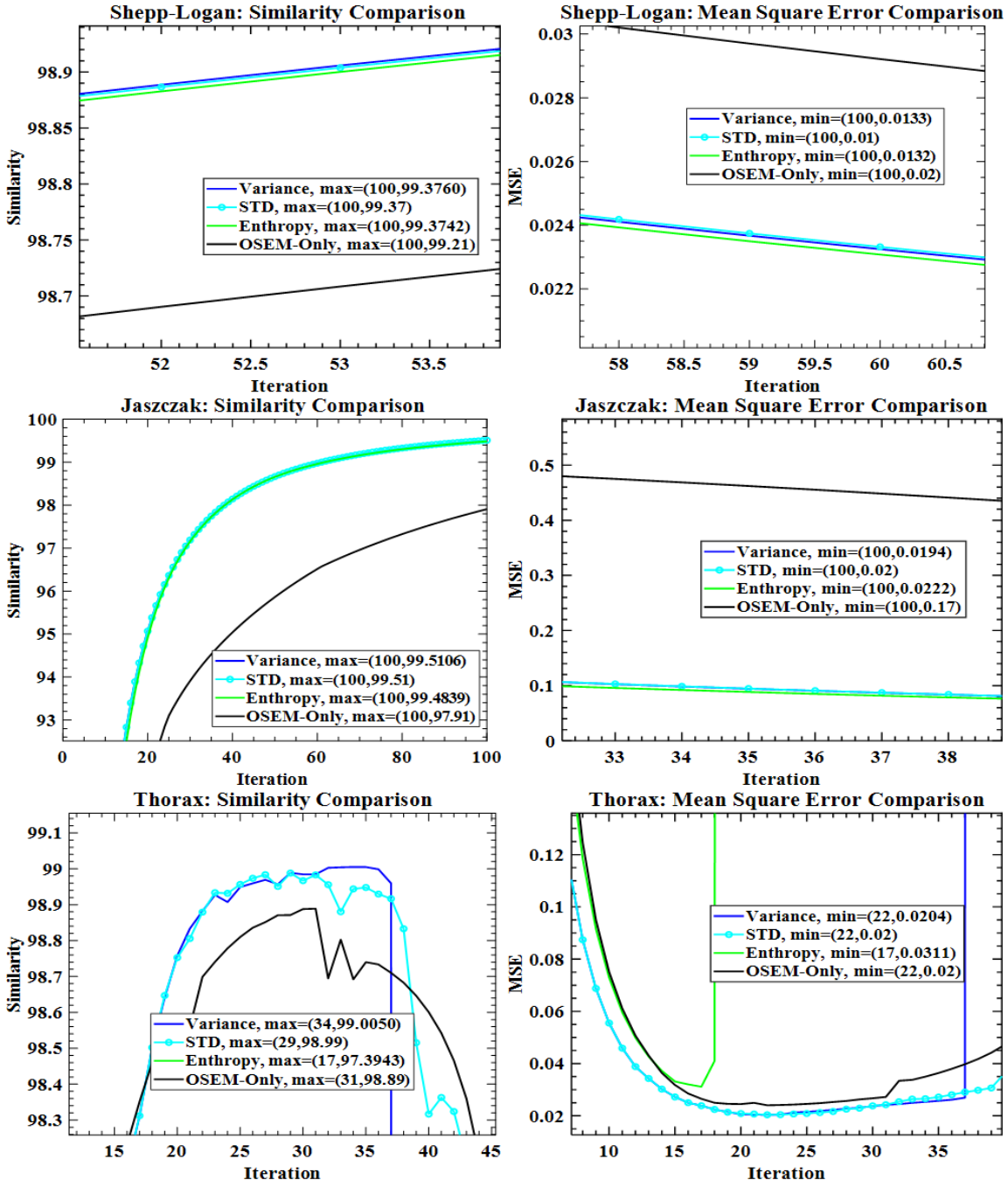

Figure 5-11: Zoom in figures of Figure 5-10: SMS-OSEM versus ordinary OSEM for phantoms 1-3 (rows 1-3 respectively): Similarity comparison (left-column) and mean square error comparison (right-column).

5.11 Number of Subsets versus Similarity for SMS-OSEM and OSEM

Comparing SMS-OSM with ordinary OSEM it can be observed from Fig. 5-12 that SMS-OSEM has better similarity accuracy than ordinary OSEM as the number of subsets increases. As the number of subset increase SMS-OSEM accuracy also increases. However, OSEM accuracy decreases after few subset increments. As a result, SMS-OSEM achieved better similarity accuracy with fewer number of iterations than ordinary OSEM. Moreover, number of subsets that can be increased depends on the phantom. In case of Shepp-Logan after 15 subsets the similarity accuracy saturates, for Jaszczak phantom after 45 subsets and for Thorax phantom after 30 subsets or losing similarity accuracy.

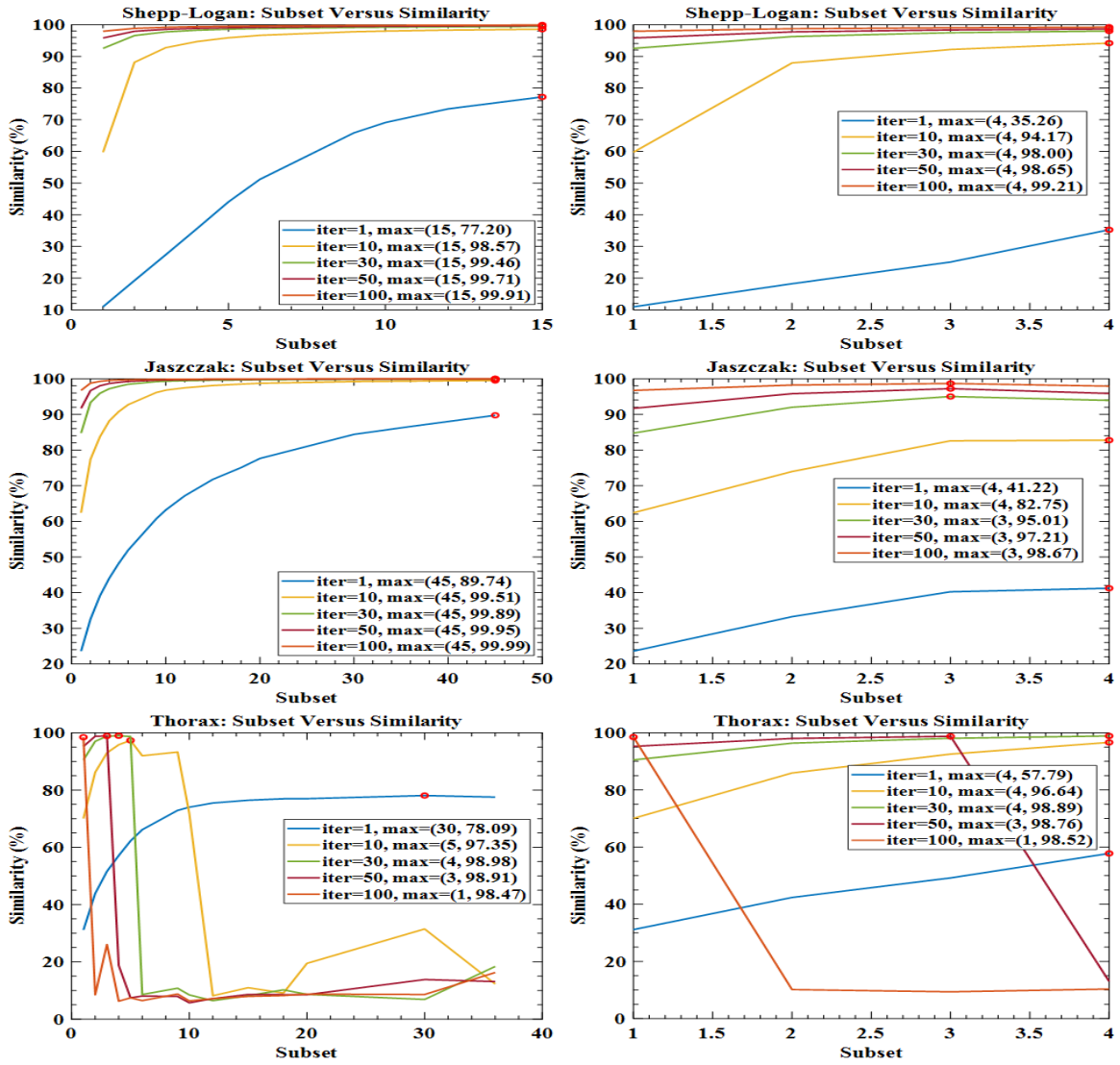

Figure 5-12: Number of Subset versus Similarity for phantoms 1-3 (rows 1-3 respectively): SMS-OSEM (left-column) versus ordinary OSEM (right-column).

5.12 Number of Subsets versus Reconstruction Time for SMS-OSEM and OSEM

Comparing SMS-OSEM and ordinary OSEM with respect to number of subsets and reconstruction time, it is observed that SMS-OSEM is faster than ordinary OSEM (see Fig. 5-13). Both SMS-OSEM and ordinary OSEM exhibit similar behavior. In both cases as the number of subsets increases, the reconstruction time decreases and then after reaching the lowest time point, the time starts to increase again. Moreover, although Thorax phantom similarity is similar for both cases (Fig. 5-12), the reconstruction time using SMS-OSEM is faster than ordinary OSEM.

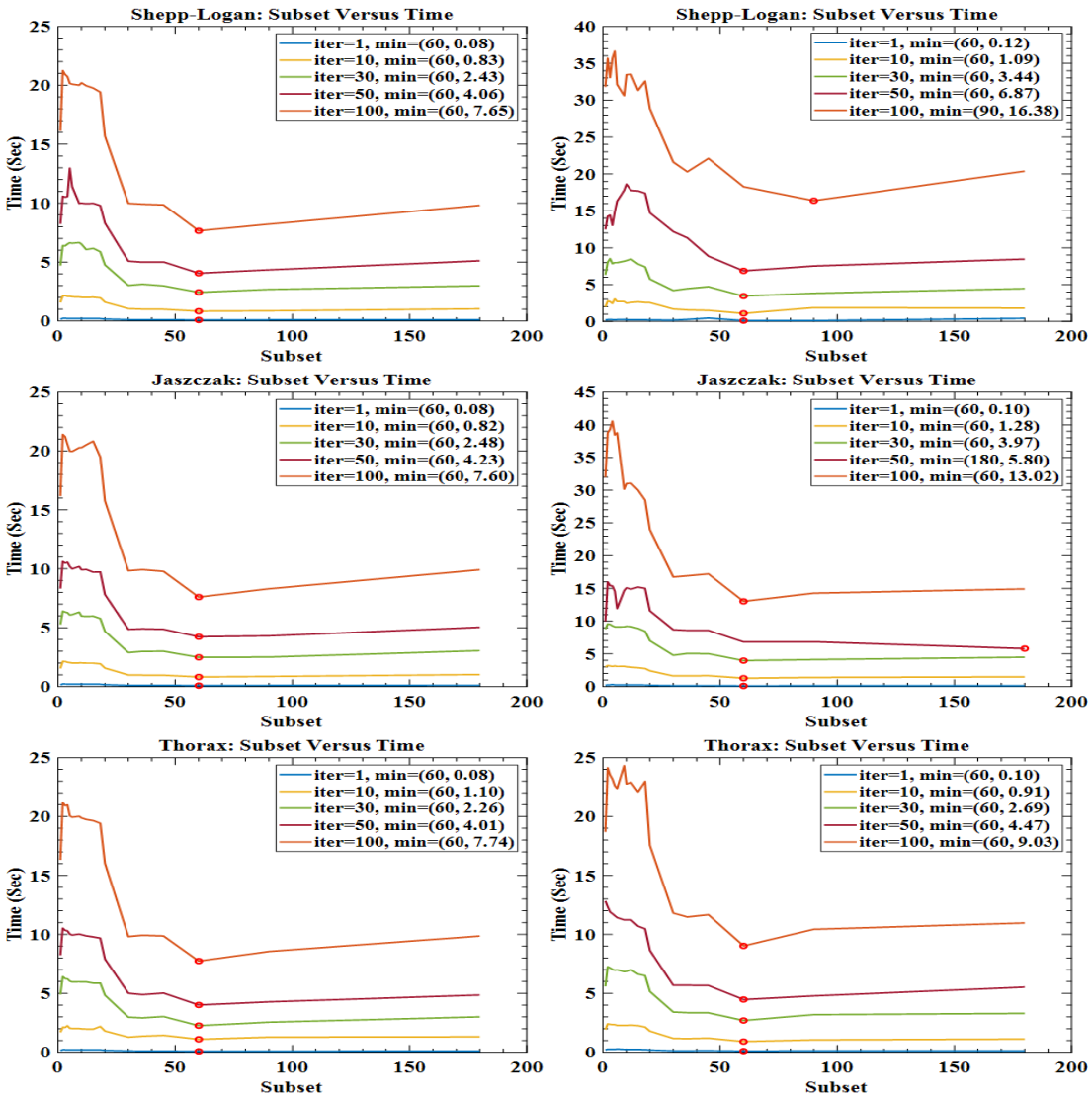

Figure 5-13: SMS-OSEM versus ordinary OSEM for phantoms 1-3 (rows 1-3 respectively): SMS-OSEM (left-column) versus ordinary OSEM (right-column).

5.13 SMS-OSEM and OSEM Comparison Summary

Analyzing the overall performance of the SMS-OSEM reconstruction and ordinary OSEM reconstruction, it can be observed (see Fig. 5-14) that SMS-OSEM out performs ordinary OSEM in terms of reconstruction time as well as reconstruction accuracy. From the result as the number of iteration increases reconstruction time increase. However, the reconstruction time of SMS-OSEM is lower than ordinary OSEM. In addition, as the number of iteration increases accuracy also increases and the SMS-OSEM accuracy is higher than OSEM. Nevertheless, for Thorax phantom as the number of iterations passes 30 iterations the similarity decreases. This shows that indefinite increment of iteration doesn't always guaranty accuracy of reconstruction.

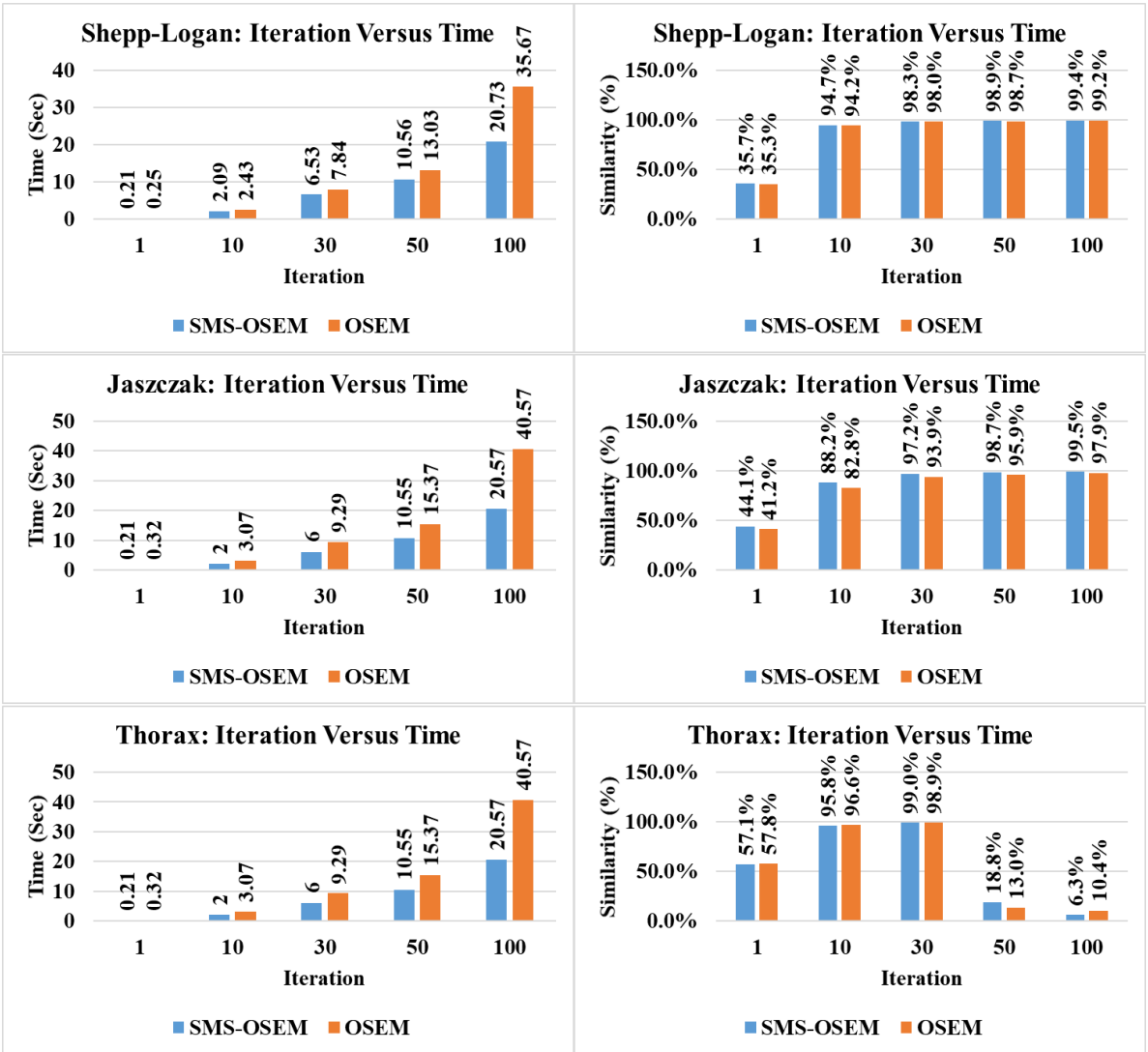

Figure 5-14: Summary of SMS-OSEM versus OSEM comparison: Iteration versus time (left column) and Iteration versus similarity (right column).

5.14 Noise Resistivity Comparison

In order to test noise resistivity of the SMS-OSEM algorithm, a Gaussian noise was added. Following this, reconstruction similarity for 100 number of iterations is computed. From the computation as shown in Fig. 5-15 in case of Shepp-Logan, the noise resistivity of the SMS-OSEM decreases after 20 iterations. However for Jaszczak and Thorax phantoms, noise resistivity of SMS-OSEM is higher (i.e. higher similarity accuracy). Hence noise tolerance is increased.

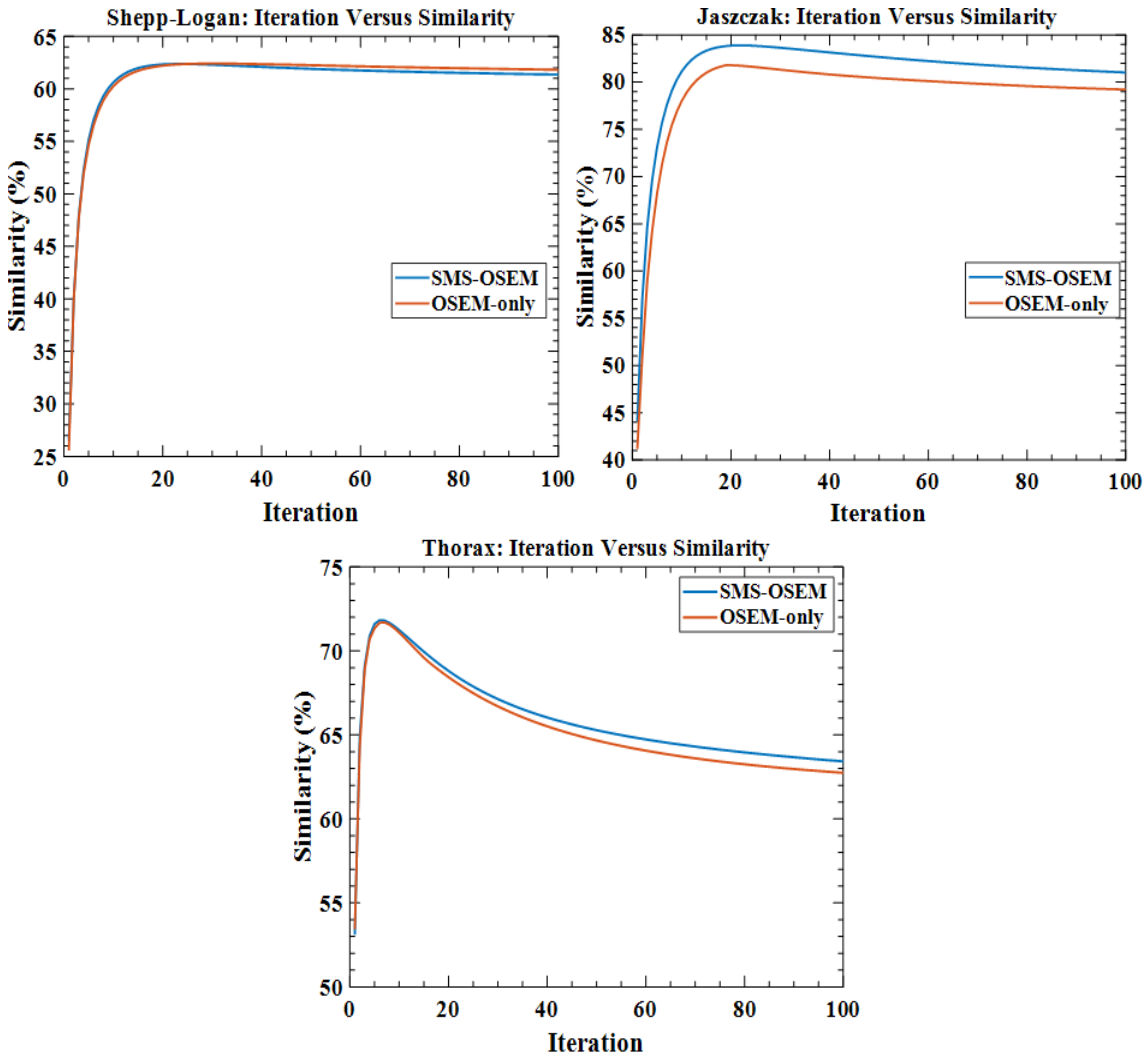

Figure 5-15: Comparison of SMS-OSEM and OSEM reconstruction for Shepp-Logan, Jaszczak and Thorax phantoms after Gaussian noise is added.

5.15 Reconstruction After Gaussian Noise Added

A Gaussian noise with mean (μ) value zero and variance (σ) value of 0.01%, 0.1%, 0.5% and 1% added to all three phantoms in order to analyze noise effect on the reconstruction. The effect of the

Gaussian noise can clearly be seen in Fig. 5-16, Fig. 5-17 and Fig. 5-18. From the figures it can be observed that except for Shepp-Logan phantom, the reconstruction accuracy of SMS-OSEM is higher than OSEM. Thus, the noise effect can be reduced by using SMS-OSEM algorithm.

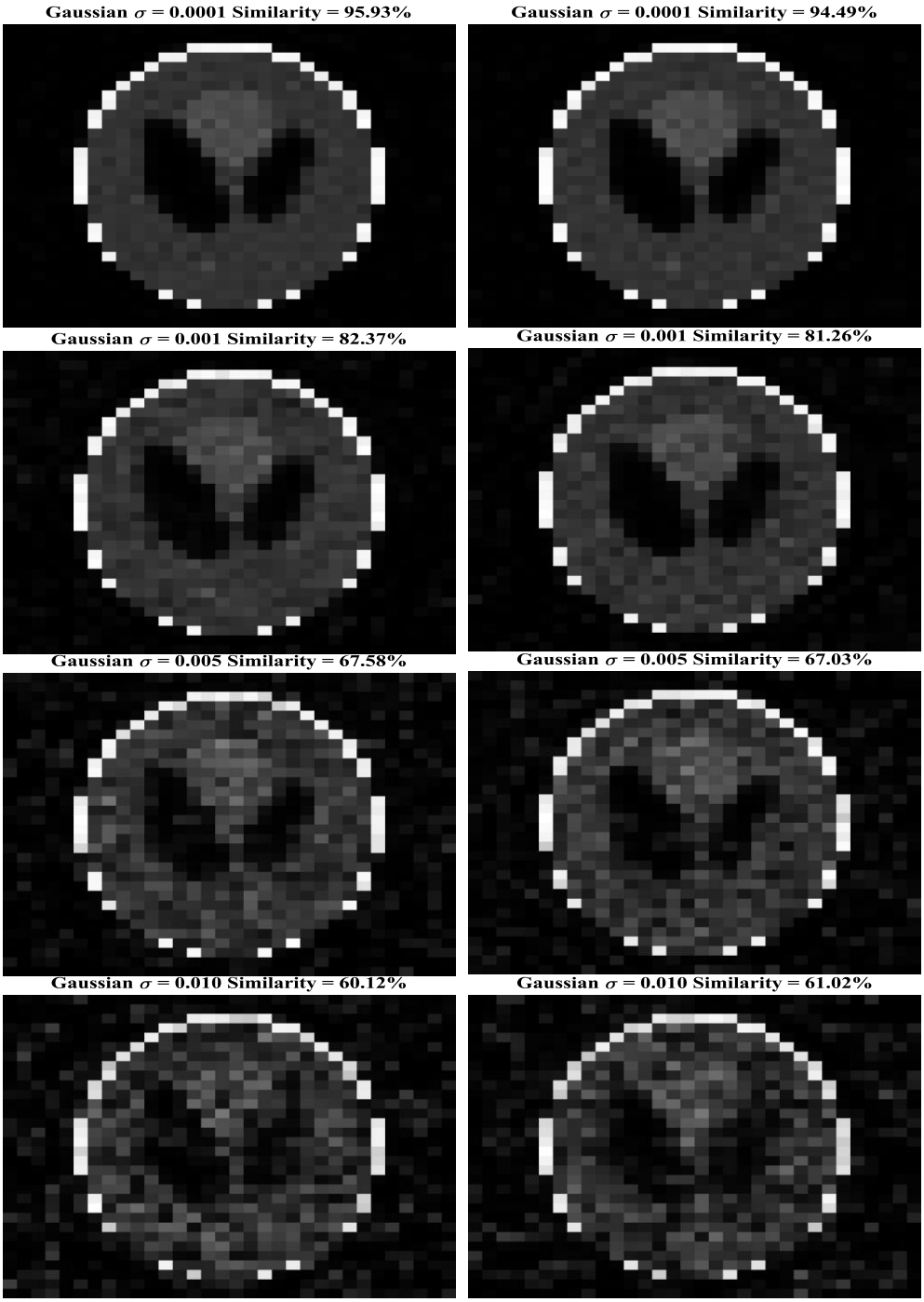

Figure 5-16: Reconstructed images of Shepp-Logan phantom, after Gaussian noise with mean (μ) zero and variance (σ) values of 0.01%, 0.1%, 0.5%, 1% respectively top to bottom are added. SMS-OSEM reconstruction (left) and OSEM reconstruction (right).

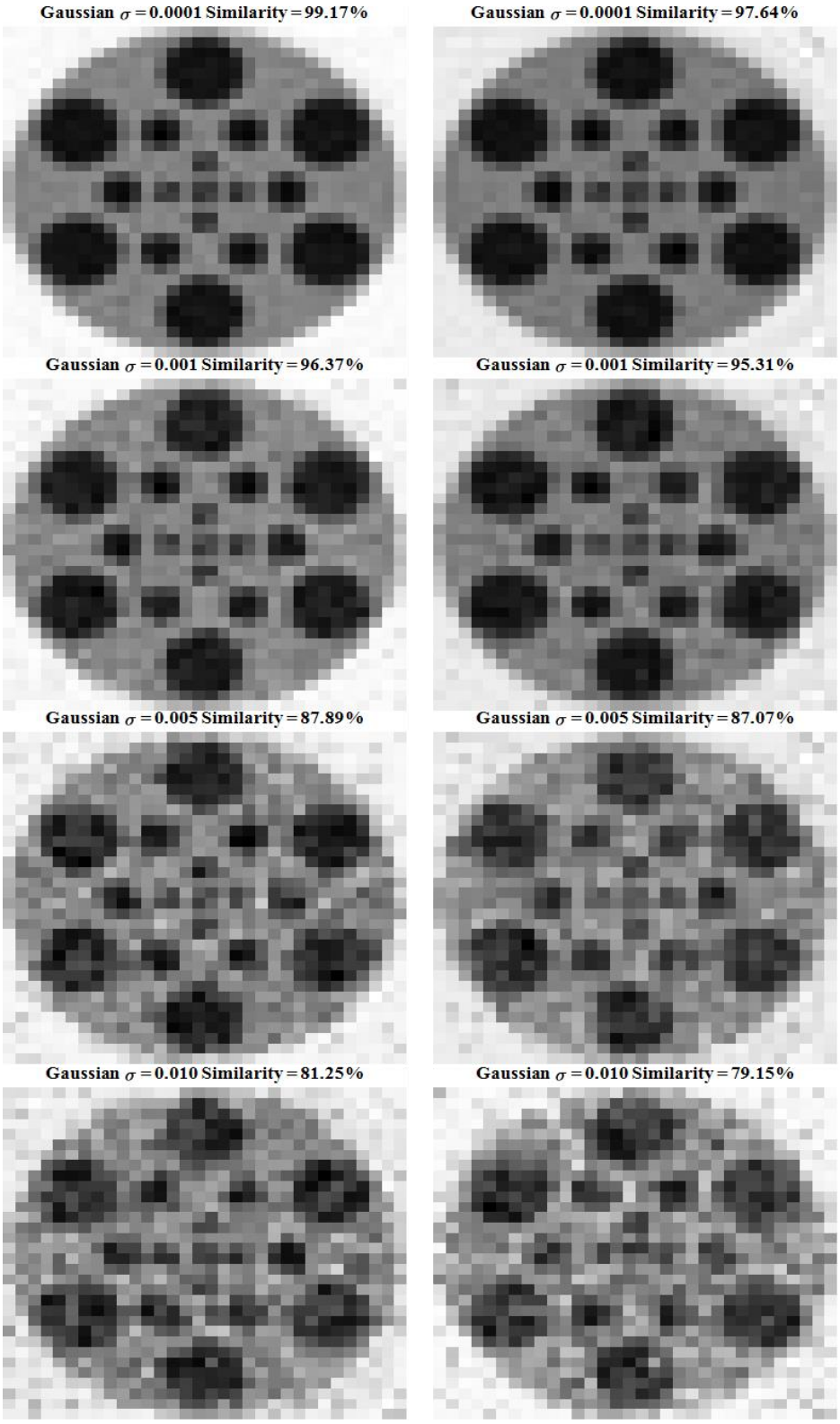

Figure 5-17: Reconstructed images of Jaszczak phantom, after Gaussian noise with mean (μ) zero and variance (σ) values of 0.01%, 0.1%, 0.5%, 1% respectively top to bottom are added. SMS-OSEM reconstruction (left) and OSEM reconstruction (right).

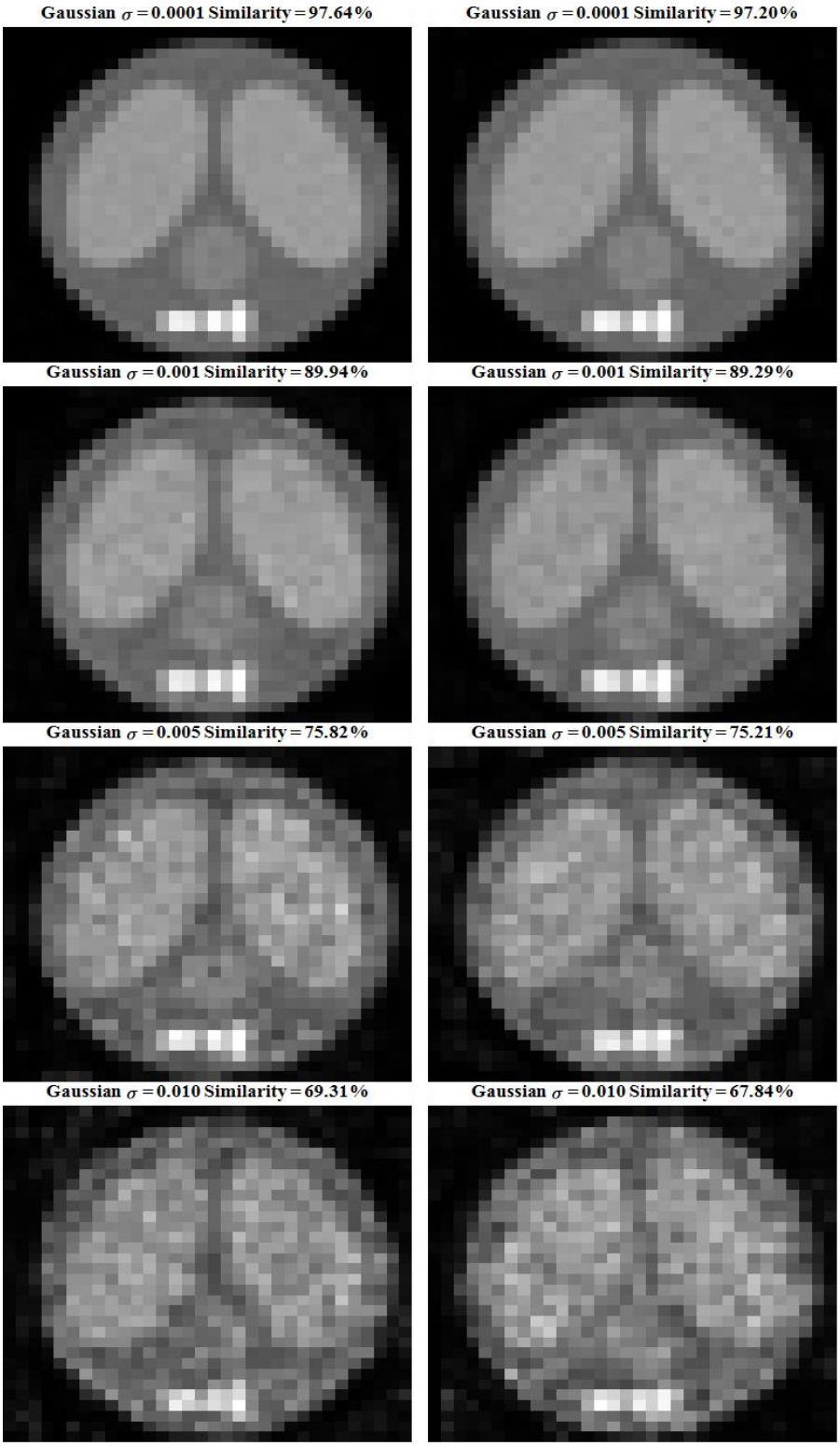

Figure 5-18: Reconstructed images of Thorax phantom, after Gaussian noise with mean (μ) zero and variance (σ) values of 0.01%, 0.1%, 0.5%, 1% respectively top to bottom are added. SMS-OSEM reconstruction (left) and OSEM reconstruction (right).

Chapter 6 Conclusion and Recommendations

6.1 Conclusion

This thesis introduced a novel technique to improve the traditional OSEM reconstruction algorithm. It is presented that by modifying the order of projection subsets based on their statistical measurement increases OSEM reconstruction accuracy and makes the reconstruction algorithm more resistant to noise that is introduced when the iteration is increased. SPECT imaging model is initially simulated. The simulation includes the SPECT imaging geometry i.e. how the SPECT rotates and how a subject is scanned. Moreover, the system probability matrix, the key factor that plays a big role in SPECT image reconstruction, is computed by analyzing the geometrical setup of the SPECT detector and the projection line relation with the image pixels. Then three phantoms were used as test images. Following this, OSEM reconstruction algorithm was applied first without modification of the subset order and then OSEM reconstruction with modification of the projection subset order. The projection subset reordering is done based on statistical measurements (variance, entropy and standard deviation) of the projection. From this it is observed that first reordering the subset determines the outcome of the image reconstruction. Second smart reordering of the projection subsets for reconstruction, i.e. giving priority for projection subsets with higher statistical value during the OSEM reconstruction, dramatically improves the accuracy of the traditional OSEM reconstruction. Not only the accuracy but also the noise resistivity due to an increase in the number of iteration is improved. Based on the three phantoms tested using statistically modified subset OSEM algorithm, it is observed that OSEM with variance based subset ordering was able to increase accuracy of ordinary OSEM reconstruction by 15.02% when the number of iteration is low between 1 and 20 iterations and for higher number of iteration 67.88% depending of the phantom type. In addition, the reconstruction time was reduced by 12.52% for lower number of iterations and by 33.03% for higher number of iterations. In addition, noise resistivity is tested by adding a Gaussian noise to the image and after reconstruction the results show that SMS-OSEM scored 2.28% offers higher accuracy than OSEM.

6.2 Recommendations for Future Work

The research that has been undertaken in this thesis has highlighted a number of topics on which further research would be beneficial. Several areas where information is lacking were highlighted in the different chapters. Whilst some of these were addressed by the research in this thesis, others remain. For instance, the SPECT collimator type was assumed parallel. More study could also be done on the phantom images reconstruction. For example, texture analysis could be applied so that preprocessing could be done before using OSEM with statistical modifications. In addition, different types of filters could also be tested to alleviate the effect of noise on the reconstruction process. Moreover, further research can be made by increasing the number of test images and using other statistical measurements in the reconstruction algorithm, which might offer a more comprehensive information about the reconstruction algorithm.

References

[1] I. Fedorov, S. Obrzut, B. Song, and B. D. Rao, “Spect image reconstruction under imaging time constraints,” in *2017 51st Asilomar Conference on Signals, Systems, and Computers*, 2017, vol. 4, pp. 1590–1594.

[2] P. P. Bruyant, “Analytic and iterative reconstruction algorithms in SPECT,” *J. Nucl. Med.*, vol. 43, no. 10, pp. 1343–1358, 2002.

[3] F. Usman, R. Zainon, A. Saidu, and A. Bala, “Evaluation of Image Reconstruction Techniques in Single Photon Emission Computed Tomography (SPECT/CT) Imaging,” *Res. Rev. J. Phys.*, vol. 5, no. 2, pp. 13–22, 2018.

[4] M. Lyra and A. Ploussi, “Filtering in SPECT image reconstruction,” *Int. J. Biomed. Imaging*, vol. 2011, 2011.

[5] & G. M. J. Mettler Jr F. A., *Essentials of nuclear medicine imaging*. Elsevier Health Sciences, 2012.

[6] B. F. Hutton, “Recent advances in iterative reconstruction for clinical SPECT/PET and CT,” *Acta Oncol. (Madr).*, vol. 50, no. 6, pp. 851–858, 2011.

[7] H. Kong, J. Pan, and Y. Han, “Evaluation of OSEM with different subset order for cone-beam CT,” *Int. J. Adv. Comput. Technol.*, vol. 5, no. 13, p. 155, 2013.

[8] S. Kawamura *et al.*, “Study on the use order of subsets in OSEM Method,” vol. 1, no. March, pp. 49–55, 2012.

[9] S. Ahmadi, H. Rajabi, F. Babapoor, and F. Kalantari, “Attenuation Correction in SPECT during Image Reconstruction using an Inverse Monte Carlo Method: A Simulation Study,” *Iran. J. Med. Phys.*, vol. 8, no. 3, pp. 1–12, 2011.

[10] R. J. Jaszczak, “The early years of single photon emission computed tomography (SPECT): an anthology of selected reminiscences,” *Phys. Med. Biol.*, vol. 51, no. 13, p. R99, 2006.

[11] S. Dorbala *et al.*, “Single Photon Emission Computed Tomography (SPECT) Myocardial Perfusion Imaging Guidelines: Instrumentation, Acquisition, Processing, and Interpretation,” *J. Nucl. Cardiol.*, vol. 25, no. 5, pp. 1784–1846, 2018, doi: 10.1007/s12350-018-1283-y.

[12] A. Rahmim and H. Zaidi, “PET versus SPECT: strengths, limitations and challenges,” *Nucl. Med. Commun.*, vol. 29, no. 3, pp. 193–207, 2008.

[13] M. M. Khalil, J. L. Tremoleda, T. B. Bayomy, and W. Gsell, “Molecular SPECT imaging: an overview,” *Int. J. Mol. Imaging*, vol. 2011, 2011.

[14] F. Laspas *et al.*, “Cardiac Magnetic Resonance versus Single-Photon Emission Computed Tomography for Detecting Coronary Artery Disease and Myocardial Ischemia: Comparison with Coronary Angiography,” *Diagnostics*, vol. 10, no. 4, p. 190, 2020.

[15] R. A. Werner *et al.*, “SPECT vs. PET in cardiac innervation imaging: clash of the titans,” *Clin. Transl. imaging*, vol. 6, no. 4, pp. 293–303, 2018.

[16] A. Cassar, D. R. Holmes Jr, C. S. Rihal, and B. J. Gersh, “Chronic coronary artery disease: diagnosis and management,” in *Mayo Clinic Proceedings*, 2009, vol. 84, no. 12, pp. 1130–1146.

[17] F. J. Bonte, T. S. Harris, L. S. Hynan, E. H. Bigio, and C. L. White III, “Tc-99m HMPAO SPECT in the differential diagnosis of the dementias with histopathologic confirmation,” *Clin. Nucl. Med.*, vol. 31, no. 7, pp. 376–378, 2006.

[18] T. A. Henderson, “The diagnosis and evaluation of dementia and mild cognitive impairment with emphasis on SPECT perfusion neuroimaging,” *CNS Spectr*, vol. 17, no. 4, pp. 176–206, 2012.

[19] J. W. Keyes, “Clinical applications of SPECT,” *Int. J. Card. Imaging*, vol. 5, no. 1, pp. 25–32, 1989.

[20] S. S. Spencer, W. H. Theodore, and S. F. Berkovic, “Clinical applications: Mri, spect, and pet,” *Magn. Reson. Imaging*, vol. 13, no. 8, pp. 1119–1124, 1995.

[21] T. Hebert and R. Leahy, “A generalized EM algorithm for 3-D Bayesian reconstruction from Poisson data using Gibbs priors,” *IEEE Trans. Med. Imaging*, vol. 8, no. 2, pp. 194–202, 1989.

[22] R. Leahy and C. Byrne, “Recent developments in iterative image reconstruction for PET and SPECT.,” *IEEE Trans. Med. Imaging*, vol. 19, no. 4, p. 257, 2000.

[23] M. Dahlbom, *Physics of PET and SPECT Imaging*. CRC Press, 2017.

[24] L. Romans, *Computed Tomography for Technologists: A comprehensive text*. Lippincott Williams Wilkins, 2018.

[25] S. R. Cherry, J. A. Sorenson, and M. E. Phelps, *Physics in nuclear medicine e-Book*. Elsevier Health Sciences, 2012.

[26] M. N. Wernick and J. N. Aarsvold, *Emission tomography: the fundamentals of PET and SPECT*. Elsevier, 2004.

[27] G. L. Zeng, *Medical image reconstruction: a conceptual tutorial.* Springer, 2010.

[28] Z. Messali, N. Chetih, A. Serir, and A. Boudjelal, "A quantitative comparative study of back projection, filtered back projection, gradient and bayesian reconstruction algorithms in computed tomography (ct)," *Int. J. Probab. Stat.*, vol. 4, no. 1, pp. 12–31, 2015.

[29] M. N. Asl and A. Sadremomtaz, "Analytical image reconstruction methods in emission tomography," 2013.

[30] J. Ram\'\irez *et al.*, "Effective emission tomography image reconstruction algorithms for SPECT data," in *International Conference on Computational Science*, 2008, pp. 741–748.

[31] A. C. Kak, M. Slaney, and G. Wang, "Principles of computerized tomographic imaging," *Med. Phys.*, vol. 29, no. 1, p. 107, 2002.

[32] T. M. Buzug, *Computed Tomography: From Photon Statistics to Modern Cone-Beam CT*. Springer Berlin Heidelberg, 2008.

[33] I. Fedorov, S. Obrzut, B. Song, and B. D. Rao, "Spect image reconstruction under imaging time constraints," *2017 51st Asilomar Conf. Signals, Syst. Comput.*, pp. 1590–1594, 2017.

[34] S. H. Al-Lehyani, "Assessment of OSEM & FBP Reconstruction Techniques in Single Photon Emission Computed Tomography Using SPECT Phantom as Applied on Bone Scintigraphy," *Sci. J. King Faisal Univ. (Basic Appl. Sci.*, vol. 10, no. 1, p. 1430, 2009.

[35] K. Lange, R. Carson, and others, "EM reconstruction algorithms for emission and transmission tomography," *J Comput Assist Tomogr*, vol. 8, no. 2, pp. 306–316, 1984.

[36] Y. Vardi, L. A. Shepp, and L. Kaufman, "A statistical model for positron emission tomography," *J. Am. Stat. Assoc.*, vol. 80, no. 389, pp. 8–20, 1985.

[37] E. A. Rashed and H. Kudo, "Statistical image reconstruction from limited projection data with intensity priors," *Phys. Med. Biol.*, vol. 57, no. 7, p. 2039, 2012.

[38] T. Yokoi, H. Shinohara, T. Hashimoto, T. Yamamoto, and Y. Niio, "Implementation and performance evaluation of iterative reconstruction algorithms in SPECT: a simulation study using EGS4," in *KEK PROCEEDINGS*, 2000, pp. 224–234.

[39] H. Zaidi, *Quantitative analysis in nuclear medicine imaging*. Springer, 2006.

[40] G. K. Loudos, "An efficient analytical calculation of probability matrix in 2D SPECT," *Comput. Med. Imaging Graph.*, vol. 32, no. 2, pp. 83–94, 2008.

[41] J. Qi and R. M. Leahy, “Resolution and noise properties of MAP reconstruction for fully 3-D PET,” *IEEE Trans. Med. Imaging*, vol. 19, no. 5, pp. 493–506, 2000.

[42] L. A. Shepp and Y. Vardi, “Maximum likelihood reconstruction for emission tomography,” *IEEE Trans. Med. Imaging*, vol. 1, no. 2, pp. 113–122, 1982.

Appendix A: Jaszczak Phantom Reconstruction Progress

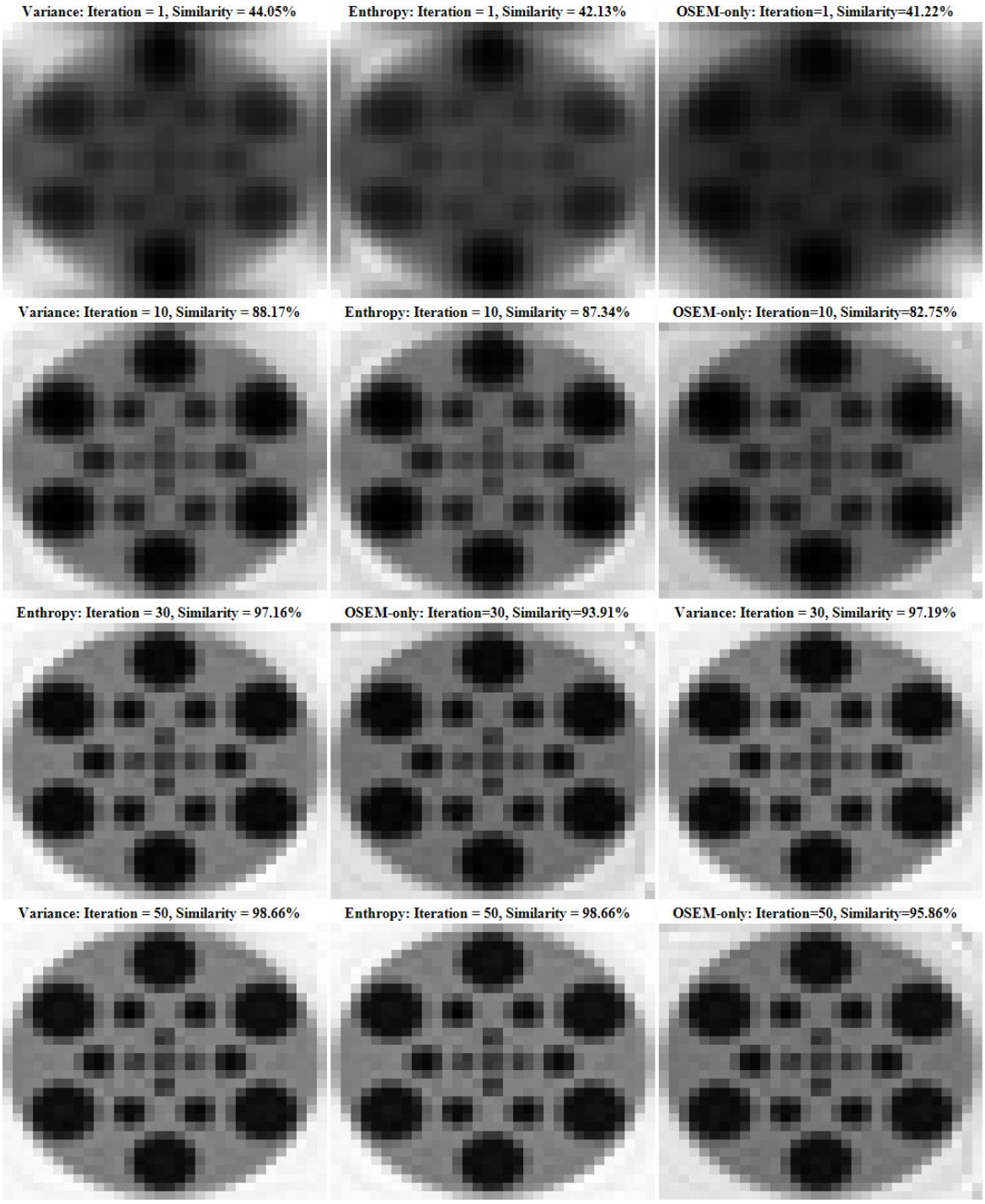

Figure A-1: Jaszczak phantom reconstruction progress: without OSEM modification (left), entropy based OSEM (middle) and variance based OSEM (right).

Appendix B: Thorax Phantom Reconstruction Progress

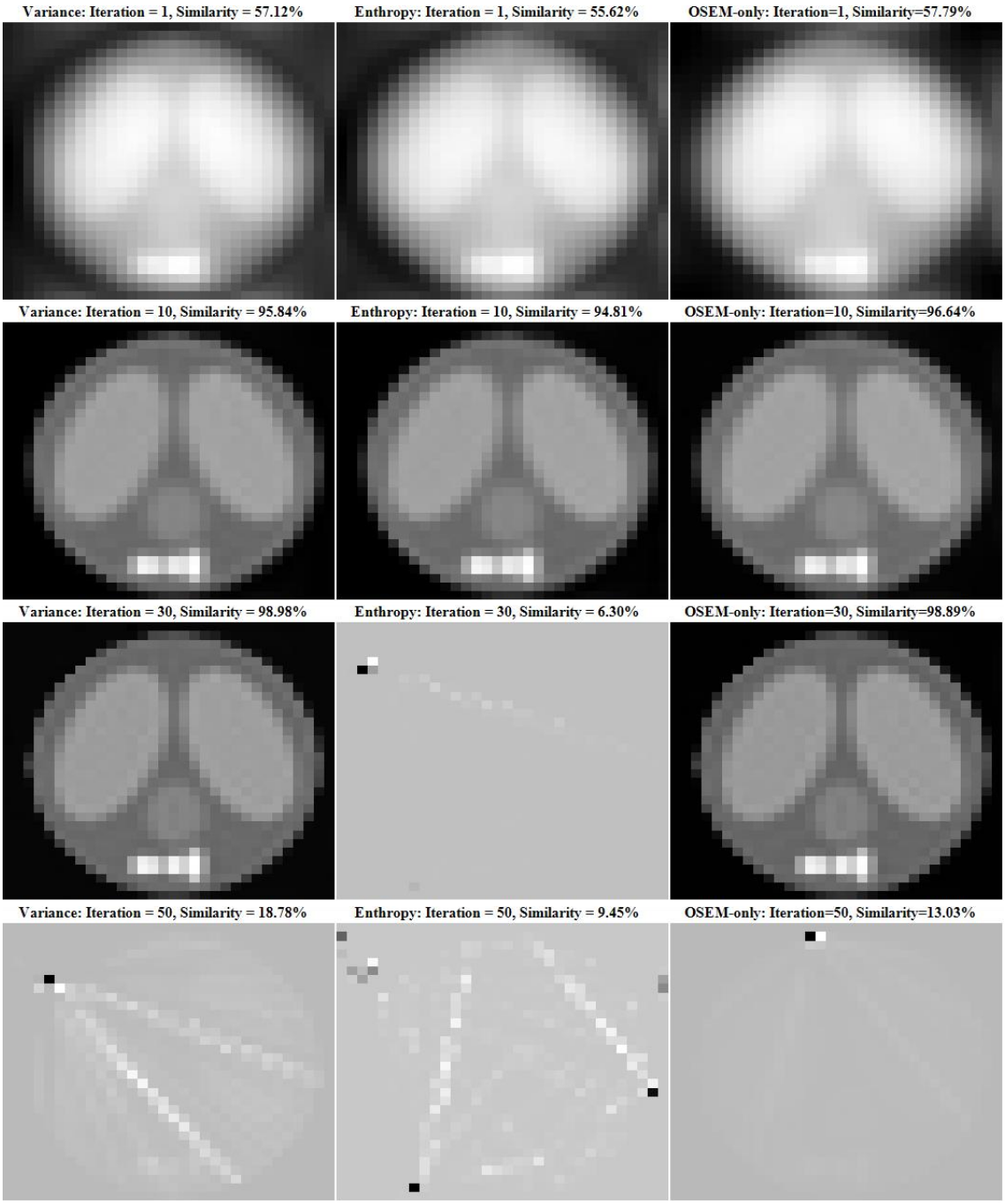

Figure B-1: Thorax phantom-3 reconstruction progress: without OSEM modification (left), entropy based OSEM (middle) and variance based OSEM (right).